MSC COMPUTATIONAL MECHANICS

Numerical Modeling of Multi-phase flow with surface tension using a level set description and X-FEM

By

LIM SHI YEE

Supervisor: Pedro Díez

Advisor: Esther Sala-Lardies

Barcelona, 28th June 2010

ABSTRACT

This document is focusing on the practical industrial applications in computational mechanics using the Extended Finite Element Method (X-FEM) to solve numerically the Navier-Stokes equation for an incompressible two-phase flow with surface tension effect. The local enrichment method enables the representation of the arbitrary jumps and kinks that are present inside the elements along the interface of two-fluid flows. The presented computational approach are basically the combination of the finite element method for spatial discretzation, the Backward Euler method for time discretization and finally the level set method for interface representation. The effect of the surface tension is carefully studied and understood in order to implement the two phase capturing method, i.e. level set technique together with the X-FEM enrichment.

Both academic and practical examples are tested with the code solving the two immiscible fluids with surface tension at the interface. An example from *J.Chessa et el.* [4], interstitial fluid in a 'Jogged' channel is presented to validate the surface tension implementation in the code. In addition, numerical results for two selected industrial applications, i.e. inkjet simulation and paper drying mechanism are presented to show the success of the method used as well as the area of improvement and potential further developments.

Keywords: Navier-Stokes equation, Multi-phase flow, surface tension, X-FEM enrichment, level set technique

ACKNOWLEDGEMENTS

First of all, I would like to thank to my thesis supervisor, Professor Pedro Díez and thesis advisor, Esther Sala – Lardies in giving me continuous support and guidance throughout the times of completing this master thesis. I am really grateful for their patience and time especially when I was stuck and had to deal with unexpected issues.

In addition, I would like to express my utmost gratitude to my comrade, Hannes Schuemann who has been working closely with me, giving me lots of encouragement and support for the past ten months. I truly appreciate his patience in sharing his knowledge, experience in programming as well as giving me clear explanation for my questions.

Besides, I would like to thank my fiancé, Jonathan Brunel and my family for their unwavering support and patience throughout this period. Also, I would like to give thousand of thanks to Charles and Elodie Dilouambaka for giving me shelter as well as continuous support during my stay in Brussels. Not to forget all my friends from Erasmus Mundus, LaCàN and ICCE, a big thank you to their time and knowledge sharing throughout the months I spent in Barcelona.

Finally, I would like to express my thanks to Lelia Zelionka from CIMNE who has been showing cares and giving support to all the Erasmus Mundus students. I truly appreciate her helpfulness each time when problems arose.

List of Tables and Figures

CONTENTS

Chapter 1

Introduction

1.1 General context

Throughout the study, it was interesting to find that surface tension effect is of high relevance in many real life phenomenon, engineering science as well as practical industrial application. From helping the insects to walk on the water to the inkjet printer that we are using every day, surface tension plays a significant role. Therefore, in the current study, surface tension is carefully studied and included in the computation in order to see its influence on the topology of the free surface as well as the interface between two immiscible fluids.

At the beginning of this master thesis, literature review and study focused on interaction of different fluids and surface tension effects. It was found that in two-fluid flows, jumps and discontinuities are presents along the interface in the velocity and pressure fields. This is because the viscosity which quantifies the relation between

velocity gradient and stresses within the fluid is most of the time different on each side of the interface (because each fluid has different material properties). This leads to a discontinuity in the velocity gradient. In addition, the surface tension force is a linear function of the local curvature of the interface. This force acts normal to the interface, in one direction only, which leads to a discontinuity in the pressure field as well. These discontinuities represent as many numerical challenges, therefore, in a second stage, we focused more specifically on solving numerically the two phase immiscible for Stokes, then Transient Stokes, and finally Navier-Stokes flows with an enriched finite element formulation. The models were tested with practical industrial applications.

1.2 Numerical approach

Interface-tracking schemes rely on modifying dynamically the mesh to capture accurately the interface; however this is usually done at the expense of lot of computational resources. In this work, the representation and evolution of the moving interface is described by the level set method which use a pure convection equation.

As explained in previous section, in two-fluid flows, jumps and kinks are presents along the interface in the velocity and pressure fields. These simulations with interface remains numerically challenging even thought various numerical methods have been developed to handle these discontinuities. Here, the well known eXtended Finite Element Method (X-FEM) is used to resolve numerically the gradient discontinuities and jumps along the interface by enriching the solution via partition of unity method. The X-FEM differentiates the unenriched elements, where the standard finite element is applied, from the fully or partially enriched elements where the approximation of the velocity is enriched with a partition of unity method.

The particularity of the method used in this study is that the level set interface capturing method is not merely used to locate the interface but is also directly used in the finite element approximations and the domain description of the X-FEM. This allows approximating the discontinuities in velocity gradient as well as provides the representation of the velocity field at the interface on the Eulerian fixed mesh. The resulting enriched velocity approximation captures the discontinuity in the velocity gradient within elements. Therefore, we could maintain the sharp interface representation even with a fixed and relatively coarse mesh.

1.3 The development of the Code

In a first time, the existing Stokes equations with surface tension implemented were rewritten into transient-Stokes. With this transient-Stokes model we conscientiously carried out a study of the surface tension effect in the formation and ejection of the droplet from the nozzle of inkjet printing device. Significant efforts has been contributed by some researchers to develop a numerical method for analyzing the inkjet process in order to find the optimal design parameters as the formation of satellites droplets is undesirable in high-quality printing. For instance, *Youngho Suh et al.*[1] and *J.A. Sethian et al.*[2]. It was found that the assumption of very low fluid velocity (advective inertial force small compared with viscous forces) was not true for this type of flows, and we had to use Navier-Stokes for this application. This is an important move as Navier-Stokes formulation is needed to solve most of the real engineering problems.

Various methods has also been tried to solve the Navier-Stokes equation. For instance, semi implicit characteristic-based split (CBS) algorithm proposed for solving incompressible multiphase flow described in Reference [3]; however it is not successfully implemented. More thorough research and study will have to be made in order to solve

the difficulties faced in implementing these methods. Finally, the semi-implicit backward Euler scheme was implemented in the code. The brief explanation on the implemented scheme is done in the introduction with the stabilization proposed by the developer.

Finally, the paper drying cylinder with turbulator bars case [2] from a technical report done by a PHD student in Finland was studied. The model was created; in a first stage the heat transfer is not considered. An attempt was made to capture the sloshing effect, but we finally focused in studying the effect of the Reynolds Number on the solution.

Chapter 2

Physical Model

2.1 Setting of the problem

The physical assumptions that we consider in our mathematical model are presented in this section. The problem is modeled as a two dimensional unsteady laminar flow of two immiscible incompressible fluids. Both the immiscible fluids are assumed to be viscous and Newtonian. A schematic diagram of two-fluid flow configuration is shown in Figure 2.1 where both the fluids are denoted as (1) and (2) with their distinct viscosities and densities.

The 2D domain Ω is bounded and partitioned into two with Ω_1 and Ω_2 separated by an arbitrary moving interface Γ_h. These domains are functions of time correspond to fluid (1) and (2) respectively.

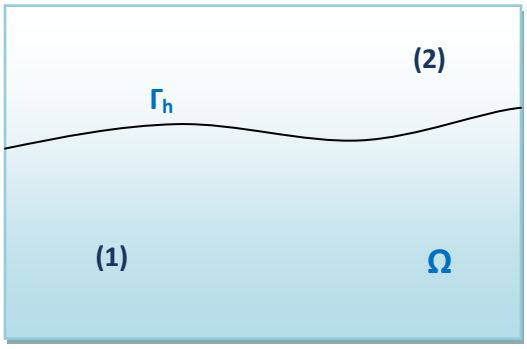

Figure 2.1 Sketch of two-fluid flow configuration in domain with interface

In addition, we consider the sharp-interface approach which simply means that the interface has zero thickness. With this assumption, the constant density and viscosity have a jump discontinuity at the interface. We also assume that surface tension effect exist on the interface with constant surface tension coefficient in tangential direction of the interface.

Lastly, we need the respective initial and sufficient boundary conditions for different problems with the proposed numerical approach in the following chapter before we start the simulations.

2.2 Navier-Stokes Formulation with Surface Tension

Taking into account all the physical assumptions, both the fluids are then governed by the incompressible Navier-Stokes equation with additional surface tension force along the interface, i.e.

$$\rho_i \frac{\partial \mathbf{u}}{\partial t} + \rho_i \mathbf{u} \cdot \nabla \mathbf{u} - \nabla \cdot \left(2\mu_i \mathbf{S}\right) + \nabla p = \rho_i \mathbf{g} + \mathbf{f}_\Gamma$$
$$\nabla \cdot \mathbf{u} = 0 \qquad in \Omega_i \quad i = 1,2 \tag{1}$$

where **u** denotes the velocity field , μ the viscosity, ***p*** the unknown pressure, **g** the acceleration of gravitational field and **S** is the deformation rate tensor, defines as $\mathbf{S} = \frac{1}{2}\left(\nabla \mathbf{u} + \left(\nabla \mathbf{u}\right)^T\right)$.

Followed by that, the surface tension force $\mathbf{f}_\Gamma$ which is the concentrated load along the interface, defined as

$$\mathbf{f}_\Gamma = \tau \kappa \delta_\Gamma \mathbf{n}_\Gamma \tag{2}$$

where τ is the surface tension coefficient between the two fluids, κ is the local curvature of the interface, δ_Γ is the Dirac delta function that localizes the surface tension force to point load on the interface and $\mathbf{n}_\Gamma$ as the unit normal to the interface.

This surface tension force balances the jump in normal stresses along the fluid interface which is denoted as $\left[\sigma \mathbf{n}\right]_\Gamma$ with the bracket denotes jumps across the interface and σ denotes the stress tensor of the Newtonian fluids, I.e. $\sigma = -pI + 2\mu S$

2.3 Dimensionless Analysis for Transient Stokes Equation

The dimensionless equation of transient Stokes equation is presented in this section. The two fluids considered are denoted as (1) and (2) as in Figure 2.1 with their viscosities and densities respectively which described by the level set function used to define the interface.

Essentially, dimensionless analysis is done to facilitate the scale-up of obtained results to real flow conditions and it enables us to check the plausibility of the derived equations used in the programming code. The dimensionless analysis done for transient Stokes equation in terms of dimensionless variables is started with the equation (1) below:

$$\begin{cases} \rho(\phi)\mathbf{u}_t - \mu(\phi)\nabla\cdot\left(\nabla^S\mathbf{u}\right)+\nabla p = \rho(\phi)\mathbf{g}+\tau\kappa\delta(\phi)\mathbf{n}, \\ \nabla\cdot\mathbf{u}=0, \end{cases} \tag{3}$$

where $\mathbf{u}$ is the velocity, μ is the viscosity, p the pressure, ρ the density, and $\mathbf{g}$ the gravitational acceleration vector. The last term in the right hand side is the surface tension force considered with τ is the surface tension coefficient, κ is the local curvature of the phase interface, $\delta(\phi)$ is the Dirac delta function that localizes the surface tension force to point load on the interface and $\mathbf{n}$ is the normal to the interface. The ∇^S is defined as $1/2\left(\nabla+\nabla^T\right)$

In order to express the above stokes equation in dimensionless form, the non dimensional variables are defined as:

$$u = V_R u^* \qquad x = L_R x^* \qquad t = T_R t^*$$

where subscript $_R$ denotes the characteristic (reference) values and asterisks denote dimensionless values respectively.

First considering the momentum equation by applying chain rule, the partial derivatives (i.e. time derivatives, pressure term, and space derivatives) in terms of dimensionless variables are computed.

The time derivative $\mathbf{u}_t = \frac{\partial \mathbf{u}}{\partial t}$ is transformed to:

$$\frac{\partial \mathbf{u}}{\partial t} = \frac{\partial V_R \mathbf{u}^*}{\partial t} = V_R \frac{\partial \mathbf{u}^*}{\partial t^*}\frac{\partial t^*}{\partial t} = \frac{V_R}{T_R}\frac{\partial \mathbf{u}^*}{\partial t^*} = \frac{{V_R}^2}{L_R}\frac{\partial \mathbf{u}^*}{\partial t^*}$$

$$\frac{\partial p}{\partial x} = \frac{\partial p}{\partial x^*}\frac{\partial x^*}{\partial x} = \frac{1}{L_R}\frac{\partial p}{\partial x^*}$$

$$\frac{\partial \mathbf{u}}{\partial x} = \frac{\partial V \mathbf{u}^*}{\partial x} = V_R \frac{\partial \mathbf{u}^*}{\partial x^*}\frac{\partial x^*}{\partial x} = \frac{V_R}{L_R}\frac{\partial \mathbf{u}^*}{\partial x^*}$$

$$\nabla \cdot (\nabla^S \mathbf{u}) = \frac{1}{L_R}\nabla^* \cdot (\frac{V_R}{L_R}\nabla^* \mathbf{u}^*) = \frac{V_R}{{L_R}^2}\nabla^* \left(\nabla^{S*} \mathbf{u}^*\right)$$

By substituting the above expressions into the momentum equation, we have:

$$\rho(\phi)\frac{{V_R}^2}{L_R}\frac{\partial u^*}{\partial t^*} = \mu(\phi)\frac{V_R}{{L_R}^2}\nabla^* \left(\nabla^{S*} \mathbf{u}^*\right) - \frac{1}{L_R}\frac{\partial p}{\partial x^*} + \rho(\phi) g - \tau\kappa\delta(\phi)\mathbf{n}$$

To continue, more dimensional variables are introduced:

$$\mu = \mu_R \mu^* \qquad \rho = \rho_R \rho^* \qquad \tau = \tau_R \tau^* \qquad g = g_R g^* \qquad p = p_R p^*$$

For the curvature κ and the normal $\mathbf{u}$, their dimension is $\frac{1}{L_R}$. Therefore, we have the dimensionless form as below:

$$\kappa = \frac{1}{L_R}\kappa^* \qquad \mathbf{u} = \frac{1}{L_R}\mathbf{u}^*$$

By substituting them into the equation, the transient Stokes equation then becomes:

$$\rho^*(\phi)\frac{\rho_R {V_R}^2}{L_R}\frac{\partial u^*}{\partial t^*} - \mu^*(\phi)\frac{\mu_R V_R}{{L_R}^2}\nabla^*\left(\nabla^{S*}\mathbf{u}^*\right) + \frac{p_R}{L_R}\frac{\partial p^*}{\partial x^*} = \rho_R\rho^*(\phi)g_R\mathbf{g} + \delta(\phi)\tau_R\tau^*\left(\frac{1}{{L_R}^2}\right)\kappa^*\mathbf{n}^*$$

Multiplying with $\frac{L_R}{\rho_R {V_R}^2}$:

$$\rho^*(\phi)\frac{\partial u^*}{\partial t^*} - \frac{\mu_R}{\rho_R L_R V_R}\mu^*(\phi)\nabla^*\left(\nabla^{S*}\mathbf{u}^*\right) + \frac{p_R}{\rho_R {V_R}^2}\nabla p^* = \left(\frac{L_R}{{V_R}^2}\right)\rho^*(\phi)g_R\mathbf{g} + \frac{\tau_R}{\rho_R L_R {V_R}^2}\delta(\phi)\tau^*\kappa^*\mathbf{n}^*$$

Introducing the Reynolds number $\mathrm{Re} = \frac{\rho_R V_R L_R}{\mu_R}$:

$$\rho^*(\phi)\frac{\partial u^*}{\partial t^*} - \frac{1}{\mathrm{Re}}\mu^*(\phi)\nabla^*\left(\nabla^{S*}\mathbf{u}^*\right) + \frac{p_R}{\rho_R {V_R}^2}\nabla p^* = \left(\frac{L_R}{{V_R}^2}\right)\rho^*(\phi)g_R\mathbf{g} + \frac{\tau_R}{\rho_R L_R {V_R}^2}\delta(\phi)\tau^*\kappa^*\mathbf{n}^*$$

Then, the similar equations hold for the y components and the continuity equation reads:

$$\nabla^* \cdot u^* = 0$$

At last, we chose to have Reynolds number for first fluid to be of value one such that:

$$\mathrm{Re} = \frac{\rho_R V_R L_R}{\mu_R} = 1, \tag{4}$$

Besides, we've also chosen the reference density and viscosity to be the physical value defined in first fluid, (i.e. ρ_1 and μ_1) in order to have a dimensionless variable of density and viscosity as described below.

$$\rho^* = \begin{cases} \dfrac{\rho_1}{\rho_R} = \begin{cases} 1 \\ \dfrac{\rho_2}{\rho_1} \end{cases} \\ \dfrac{\rho_2}{\rho_R} \end{cases} \qquad \mu^* = \begin{cases} \dfrac{\mu_1}{\mu_R} = \begin{cases} 1 \\ \dfrac{\mu_2}{\mu_1} \end{cases} \\ \dfrac{\mu_2}{\mu_R} \end{cases}$$

Then, by giving the choice to the user to define the value for the characteristic length, L_R we can have the characteristic velocity defined as:

$$V_R = \frac{\mu_1}{\rho_1 L_R}$$

Finally by setting the reference values for pressure, surface tension coefficient and gravity force as written below:

$$\tau_R = \rho_R L_R V_R^{\,2} \qquad g_R = \frac{V_R^{\,2}}{L_R} \qquad p_R = \rho_R V_R^{\,2}$$

We could come up with the dimensionless form as below:

$$\rho^*(\phi)\frac{\partial u^*}{\partial t^*}-\frac{1}{\mathrm{Re}}\mu^*(\phi)\nabla^*\left(\nabla^{S*}\mathbf{u}^*\right)+\nabla p^*=\rho^*(\phi)\mathbf{g}+\delta(\phi)\tau^*\kappa^*\mathbf{n}^*$$

The dimensionless transient Stokes problem (with omitted *) could be written as:

Find $\mathbf{u}$ and p such that:

$$\begin{cases}\rho(\phi)\dfrac{\partial \mathbf{u}}{\partial t}-\dfrac{1}{\mathrm{Re}}\mu(\phi)\nabla\left(\nabla^{S}\mathbf{u}\right)+\nabla p=\rho(\phi)\mathbf{g}+\delta(\phi)\tau\kappa\mathbf{n}\\ \nabla\cdot\mathbf{u}=0\end{cases} \tag{5}$$

Chapter 3

Numerical Approach

In this section, the numerical implementation for the computation of the two phase incompressible flows with surface tension is presented. The front capturing method which is called the level set method is applied to solve two-phase incompressible flows with the ability to capture the changes of the topology correctly. The interface is captured by level set function which is defined as a signed distance function and is approximated by the same finite element mesh.

The discontinuity in the derivative of velocity is enriched by introducing the Ridge Function where its gradient is discontinuous across the interface while the Heaviside function is added to handle the pressure jump along the fluid interface. Therefore, this finite element method requires no re-meshing and allows the interface to move arbitrarily throughout the whole mesh.

3.1 Level Set Method for Two Phase incompressible flow

A front capturing method which is called the level set method is used to solve two-phase incompressible flows with the ability to capture the changes of the topology correctly. This method defines a smooth distance function, $\phi(\mathbf{x},t)=0$ where it is positive in one region and negative in another. Then, the zero level of this function indicates the current position of the interface, which is:

$$\phi(\mathbf{x},t)=\begin{cases}-d\ , for & x & in & \Omega_1\\ 0\ \ , for & x & on & \Gamma\\ d\ \ , for & x & in & \Omega_2\end{cases} \tag{11}$$

with d as the distance of the set of points in $\mathbf{x}$ from interface.

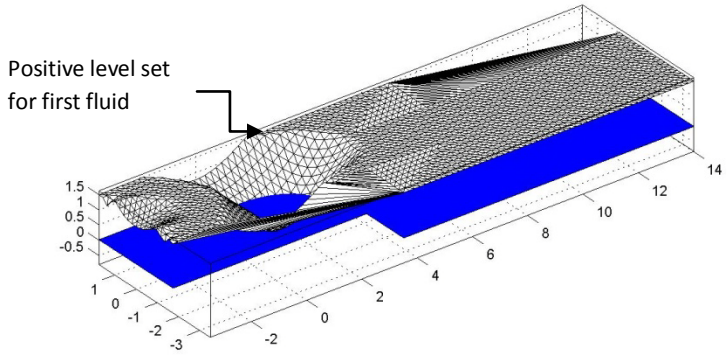

Figure 3.1 Level set at time step 20 of interstitial fluid problem showing interface, positive and negative level set

In each time step, the level set function is advected by a velocity field of the fluid, along with the fluid materials, which is the solution of the Navier-Stokes equations of the two phase flows that we are solving. The scalar advection equation for the interface is as shown as followed:

$$\partial_t \phi + \mathrm{u} \cdot \nabla \phi = 0 \tag{12}$$

Due to the fact that the velocity field is the known solution, thus level set is then transported by integrating equation (12) with the two-step third order Taylor-Galerkin method (2S-TG3) introduced in [21]. This method is an explicit time marching scheme which requires significantly small time step size in moving the level set to ensure stability of this scheme. Further explanation on the implementation of this scheme can be found in [21].

The same function is then used to define the densities and viscosities of the fluids, they are:

$$\rho(\mathbf{x}) = \begin{cases} \rho_1, & for \quad \phi > 0 \\ \rho_2, & for \quad \phi < 0 \end{cases}$$

$$\mu(\mathbf{x}) = \begin{cases} \mu_1, & for \quad \phi > 0 \\ \mu_2, & for \quad \phi < 0 \end{cases}$$

In order to maintain this level set function as a distance function always, i.e. to have the accurate representation of the interface, reinitialization and smoothing of level set is included in the code. Here, the reinitialization is applied after certain number of time steps. It is meant to rebuild the sign distance function which gets inaccurate when we move the level set.

As for the smoothing of level set, a tuning parameter ε was implemented in the code. It introduces artificial diffusion to the level set function. It is important to note that all the results shown in this thesis used a version of the code where the smoothing parameter was made linear function of the mesh size. Therefore, for a big mesh size, the smoothing effect was increased and for a small element the smoothing effect is reduced. The idea

being that coarse mesh would tend to destabilize the interface tracking scheme and lead to spurious results. However, this relies on an optimistic assumption that smoothing can completely overcome the effect of the mesh coarseness. In the case where the level set function fail on coarse mesh (with higher smoothing), making the smoothing a function of the mesh size means does not allow to refine the mesh and keep the same smoothing. In the worst case, the effect of the mesh refinement on the level set method could even be canceled by the effect of the decrease in smoothing.

3.2 Space Discretization with X-FEM

The Navier-Stokes equation (1) is being discretized using a mixed formulation into elements with a set of nodes where the velocity and pressure are interpolated differently with their corresponding shape functions. In order to fulfill the LBB condition which ensure the stability of this formulation, Q2Q1 (Taylor-Hood Element) and P2P1 elements are used. Both the elements have continuous biquadratic velocity and continuous bilinear pressure. They satisfy the inf-sup or LBB condition with quadratic convergence.

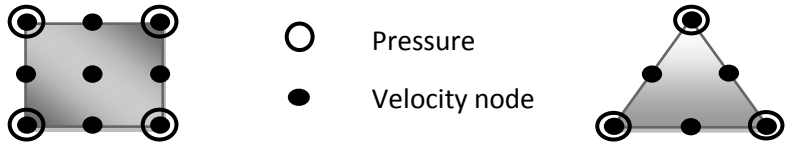

(a) (b)

Figure 3.2 Types of elements used with (a) Q2Q1 elements and (b) P2P1 elements

For the enriched finite element approximation, a special treatment is given for the enriched elements (elements which are intersected by the interface) as well as the blended

elements (element with partially enriched nodes). The additional interpolation function (shape function) is added to the enriched nodes mentioned above. For the rest of the nodes, the standard finite element interpolation will be applied.

For velocity interpolation, Ridge function $R(x)$ (13) is added to represent the discontinuous velocity gradient on the interface. As for the pressure interpolation, a step function which is called Heaviside function $H(\phi(x))$ (14) is used to enrich the pressure discretization along the interface.

$$R(x) = \sum_{j \in \square_{enr}} \left|\phi_j\right| N_j(x) - \left| \sum_{j \in \square_{enr}} \phi_j N_j(x) \right| \tag{13}$$

$$H(\phi(x)) = \begin{cases} 1 & for \quad \phi > 0 \\ 0 & for \quad \phi \le 0 \end{cases} \tag{14}$$

Thus, the enriched interpolations of velocity and pressure are expressed in (15) and (16) below.

$$u_h(x,t) = \sum_{j \in \square_u \square_{enr}} u_j(t) N_j^u(x) + \sum_{j \in \square_{enr}} a_j(t) R(x) N_j^u(x) \tag{15}$$

$$p_h(x,t) = \sum_{j \in \square_p \square_{enr}} p_j(t) N_j^p(x) + \sum_{j \in \square_{enr}} b_j(t) H(x) N_j^p(x) \tag{16}$$

Where a_j and b_j are the additional degrees of freedom introduced by the enrichment functions for velocity and pressure respectively.

3.3 Semi-implicit Backward Euler Time Discretization

The Navier-Stokes Equation which governed the fluids is being described, i.e. the semi implicit Backward Euler Approach. Given the strong form of the problem, find the velocity field ***u*** and the pressure field *p*, such that:

$$\begin{cases} \rho_i \dfrac{\partial \mathbf{u}}{\partial t} + \rho_i \mathbf{u} \cdot \nabla \mathbf{u} - \mu_i \nabla \cdot \left(\nabla^S \mathbf{u} \right) + \nabla p = -\rho_i \mathbf{g} + \tau \kappa \mathbf{n} & in \quad \Omega \\ \nabla \cdot \mathbf{u} = 0 & in \quad \Omega \\ \mathbf{u} = \mathbf{u}_D & on \quad \partial\Omega \end{cases} \tag{6}$$

where $\mathbf{u}$ is the velocity, μ_i is the viscosity, ρ_i the density, $\mathbf{g}$ the gravitational acceleration vector, τ the surface tension coefficient and $\mathbf{u}_D$ the Dirichlet boundary conditions. Only the Dirichlet boundary conditions $\mathbf{u}_D$ are imposed in this problem. The velocity boundary conditions are imposed everywhere on $\partial\Omega$. We also fix one degree of freedom for the pressure if the flow problem is confined.

As for the time discretization used for velocity field in the first term of equation 3.1 described above, the first order accurate Backward Euler discretization is used. The equation reads:

$$\frac{\partial \mathbf{u}}{\partial t} = \frac{\mathbf{u}^{n+1} - \mathbf{u}^n}{\Delta t} \tag{7}$$

Where the $\mathbf{u}^{n+1}$ is the velocity of the current time step and $\mathbf{u}^n$ the velocity from previous time step. Backward Euler is an implicit method which gives unconditional stability

where the pressure and velocity would be solved for n+1 time step. However, in this work we are solving it in a 'semi-implicit' way. By saying this, we replaced the non-linear convection term ($\mathbf{u}^{n+1}\cdot\nabla\mathbf{u}^{n+1}$) as ($\mathbf{u}^{n}\cdot\nabla\mathbf{u}^{n+1}$) by approximating the solution of the velocity from previous time step. With this semi-implicit approximation, we then have the momentum equation and the incompressibility c as shown below.

$$\frac{1}{\Delta t}\rho_i\mathbf{u}^{n+1}+\rho_i\mathbf{u}^{n}\cdot\nabla\mathbf{u}^{n+1}-\mu_i\nabla\cdot\left(\nabla^{S}\mathbf{u}^{n+1}\right)+\nabla p^{n+1}=\frac{1}{\Delta t}\rho_i\mathbf{u}^{n}+\rho_i\mathbf{g}+\tau\kappa\mathbf{n} \qquad in \quad \Omega$$

$$\nabla\cdot\mathbf{u}^{n+1}=0 \qquad in \quad \Omega$$

$$\mathbf{u}^{n+1}=\mathbf{u}_D(t) \qquad on \quad \partial\Omega \qquad (8)$$

3.4 The Weak Form

The weak formulation is obtained by multiplying the equation with a test function $w\in V$ in space as well as $q\in Q$ for the incompressibility condition. Integrating all the terms over the full domain Ω and we would get as follow:

$$-\frac{1}{\Delta t}\left(\rho_i\mathbf{u}^{n+1}\right)=-\frac{1}{\Delta t}\int_\Omega w^{n+1}\cdot\rho_i\mathbf{u}^{n+1} \quad d\Omega$$

$$\rho_i\mathbf{u}^{n}\cdot\nabla\mathbf{u}^{n+1}=\int_\Omega w^{n+1}\cdot\rho_i\mathbf{u}^{n}\cdot\nabla\mathbf{u}^{n+1} \quad d\Omega$$

$$-\mu_i\nabla\cdot\left(\nabla^{S}\mathbf{u}^{n+1}\right)=\int_\Omega w^{n+1}\cdot\left(\mu_i\nabla\cdot\left(\nabla^{S}\mathbf{u}^{n+1}\right)\right) \quad d\Omega$$

$$\nabla p^{n+1}=\int_\Omega w^{n+1}\cdot\nabla p^{n+1} \quad d\Omega$$

$$\frac{1}{\Delta t}\rho_i \mathbf{u}^n = \frac{1}{\Delta t}\int_\Omega w^{n+1}\rho_i \mathbf{u}^n \quad d\Omega$$
$$\left(\rho_i \mathbf{g}\right) = \int_\Omega w^{n+1}\cdot \rho \mathbf{g} \quad d\Omega$$
$$\tau\kappa\mathbf{n} = \int_\Gamma w^{n+1}\cdot \tau\kappa\mathbf{n} \quad d\Gamma$$

For viscous term, integration by parts and Green-Gauss divergence theorem is applied and rewritten as below:

$$\int_\Omega w^{n+1}\cdot\left(\mu_i\nabla\cdot\left(\nabla^S\mathbf{u}^{n+1}\right)\right)d\Omega = \int_\Omega \nabla w^{n+1} : \left(\mu_i\nabla^S\mathbf{u}^{n+1}\right)d\Omega + \int_{\Gamma_N} w^{n+1}\left(\mu_i\nabla^S\mathbf{u}^{n+1}\right)\cdot\mathbf{n}$$

In the same way, we applied the theorems for the pressure gradient term and we get,

$$\begin{aligned}\int_\Omega w^{n+1}\cdot\nabla p^{n+1}d\Omega &= \int_\Omega \nabla\cdot(w^{n+1}p^{n+1})d\Omega - \int_\Omega p^{n+1}\nabla\cdot w^{n+1}d\Omega \\ &= \int_{\partial\Omega}(w^{n+1}p^{n+1})\mathbf{n}d\Omega - \int_\Omega p^{n+1}\nabla\cdot w^{n+1}d\Omega\end{aligned}$$

Finally the weak formulation of Navier-Stokes equation for two-phase incompressible flow in a gravitational field with surface tension together with the incompressibility condition can be expressed as followed.

$$\begin{aligned}&-\frac{1}{\Delta t}\int_\Omega w^{n+1}\cdot\rho_i\mathbf{u}^{n+1} \quad d\Omega + \int_\Omega w^{n+1}\cdot\rho_i\mathbf{u}^n\cdot\nabla\mathbf{u}^{n+1} \quad d\Omega \\ &\quad + \int_\Omega \nabla w^{n+1} : \left(\mu_i\nabla^S\mathbf{u}^{n+1}\right)d\Omega - \int_\Omega p^{n+1}\nabla\cdot w^{n+1}d\Omega \\ &\qquad = \frac{1}{\Delta t}\int_\Omega w^{n+1}\rho_i\mathbf{u}^n \quad d\Omega + \int_\Omega w^{n+1}\cdot\rho\mathbf{g} \quad d\Omega + \int_\Gamma w^{n+1}\cdot\tau\kappa\mathbf{n} \quad d\Gamma\end{aligned} \tag{9}$$

And

$$\int_\Omega \nabla\cdot q^{n+1}\cdot\mathbf{u}^{n+1} = 0 \tag{10}$$

Chapter 4

Code Applications in Surface Tension Effects

4.1 Effects of the Surface Tension tested on Transient Stokes Dimensionless Equation

In this section, we are only interested in testing the implementation of the surface tension term inside the code. Therefore, we are using the Dimensionless Transient Stokes Equation without having to care for the non-linear convection term. Here, the example problem 6.1 in *Chessa et al.* [18] interstitial fluid in a "jogged" channel was adopted to perform the implementation of surface tension in the code. This example was used by *Chessa et al.* to demonstrate the implementation of X-FEM to resolve the velocity gradient discontinuity in two-phase fluids together with the evolution of interface in time by front capturing level set method. In Figure 4.2, the steady state velocity field and interface at several time-steps for interstitial fluid presented by *Chessa et al.* is shown and the results are compared subsequently. However, it is mentioned in the publication that In

this section, it is also used to show the effects of surface tension with different Reynolds number, i.e. the ratio of density and viscosity of one respectively. Besides, this example is also tested with different material properties of both the fluids. This is intended to see how the code would handle the problems with big density ratio as well as viscosity ratio. The initial configuration of this problem is shown in Figure 4.1. The inlet velocity $u_x = u(t)$ is prescribed at the entrance of the channel.

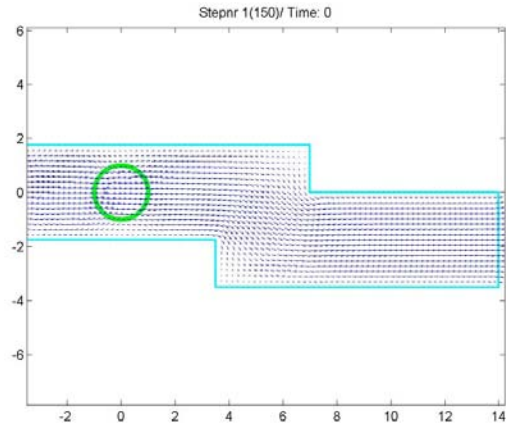

Figure 4.1 The first time step of the bubble in jogged channel flow

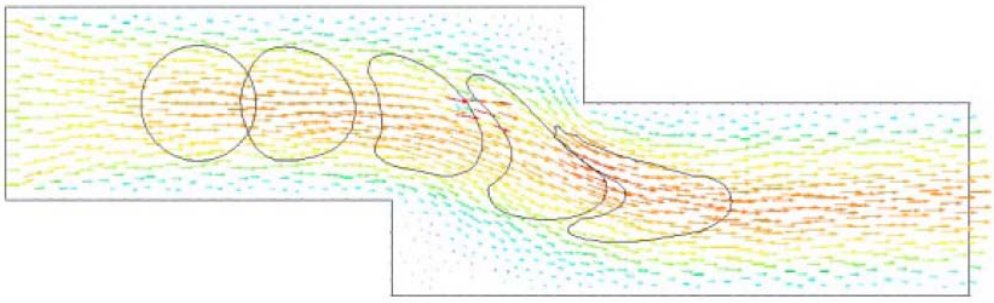

Fig. 7 Phase interface at several time-steps for interstitial fluid problem

Figure 4.2 Interface at several time-steps for interstitial fluid problem in *Chessa et al.*

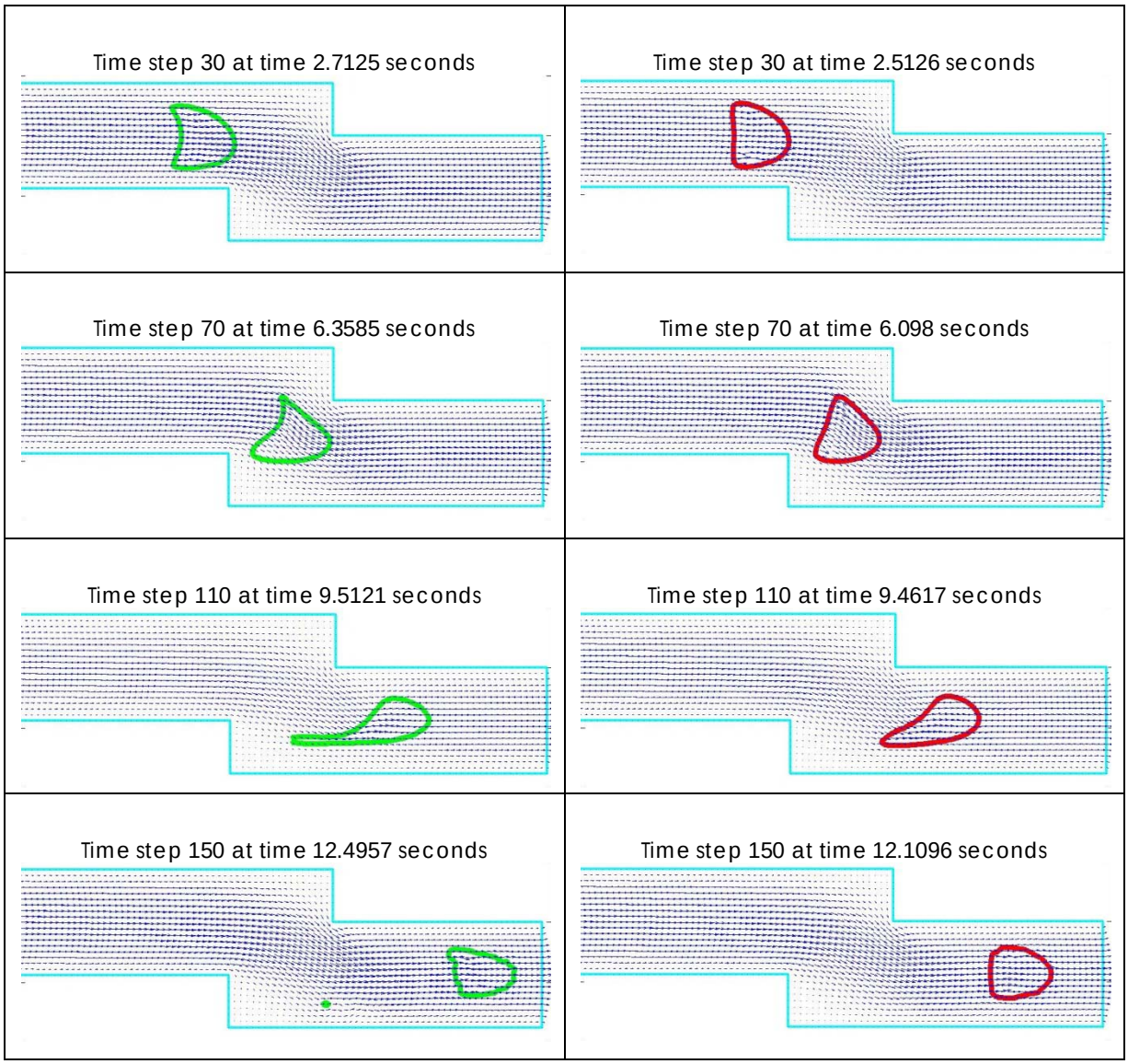

Table 4.1 Comparison of results for flow at Reynolds number 10 for both fluids at (a) τ = 0.25 and (b) τ = 0.75

This example clearly shows the effects of surface tension coefficient, τ by using the same Reynolds number for both fluids. With the Reynolds number of 10 for both fluids and a lower τ, the bubble tent to deform more compare to the results for a higher τ at reasonably same time. The interface has been captured nicely

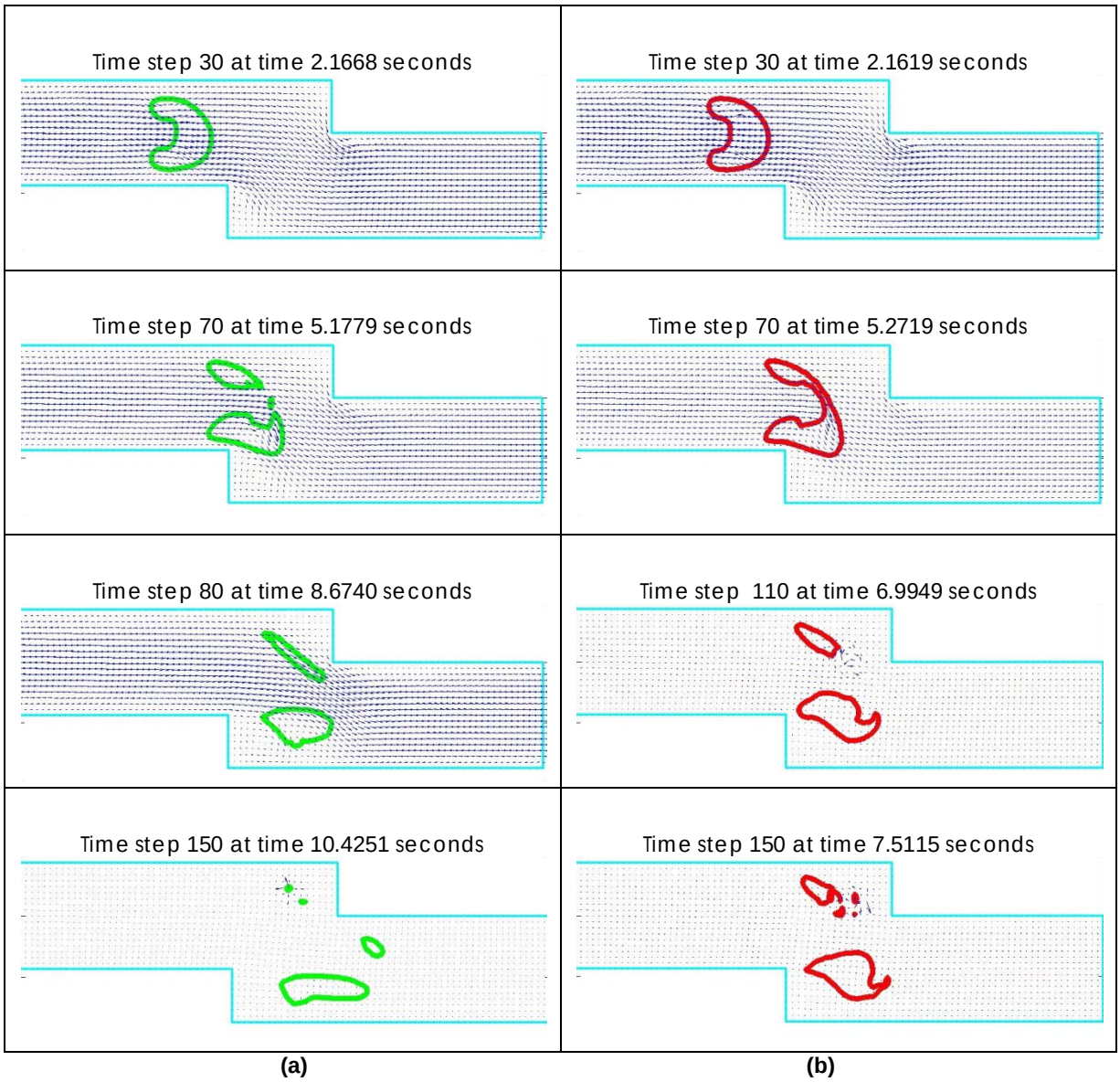

Table 4.2 Velocity plots with Reynolds number 100 for both fluids at (a) $\tau = 0.25$ and (b) $\tau = 0.75$

For the second computation results shown in Table 4.2 above, with higher Reynolds number for both the fluids, it means that less viscosity is present. Therefore, it seems convincing that we have the separation happened at time step 150 for $\tau = 0.75$ compared to the results obtained for flows with Reynolds number 10. From the interface

plots for both τ we can see that the interface could not be captured properly. It is admitted that the stability of the code is again challenged to handle high Reynolds number flows.

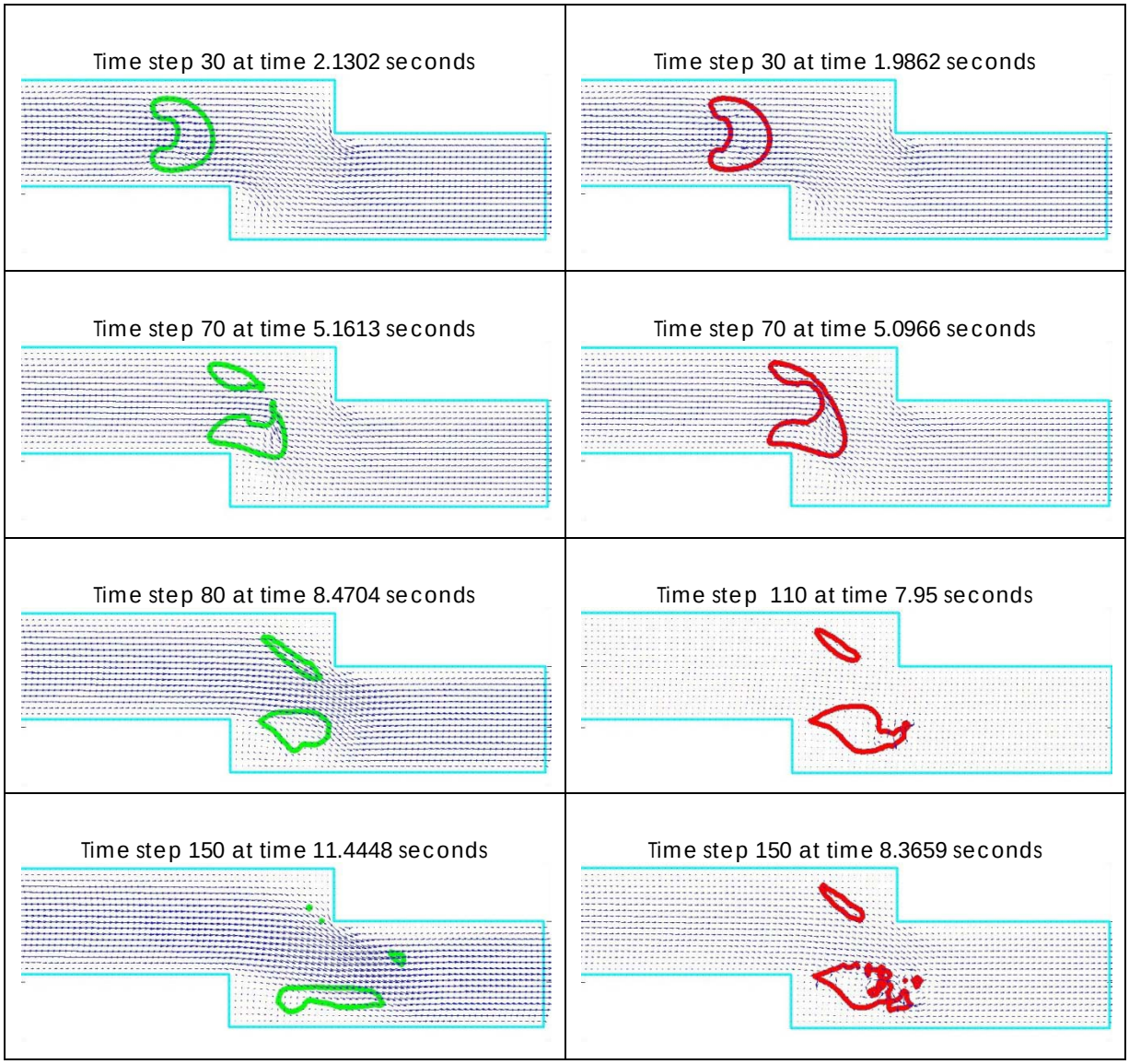

Table 4.3 Velocity plots with Reynolds number 100 for fluid 1 and Reynolds number 10 for fluid2 (bubble) with (a) τ = 0.25 and (b) τ = 0.75

Next, a computation with different Reynolds number has been done to further study the effects of surface tension for the bubble in the jogged channel. It is found that the interface capturing by the level set has been somehow corrupted at time step 110 for results with τ =0.75 after the separation happened on the bubble. We can conclude that at this stage, the stability of the code has to be further studied to handle high Reynolds number fluids as well as fluids with big density and viscosity differences.

Generally, we can see a good mass conservation is obtained from the various computations done. Therefore, it is then moved further to Navier-Stokes formulation where the non-linear viscous term is introduced.

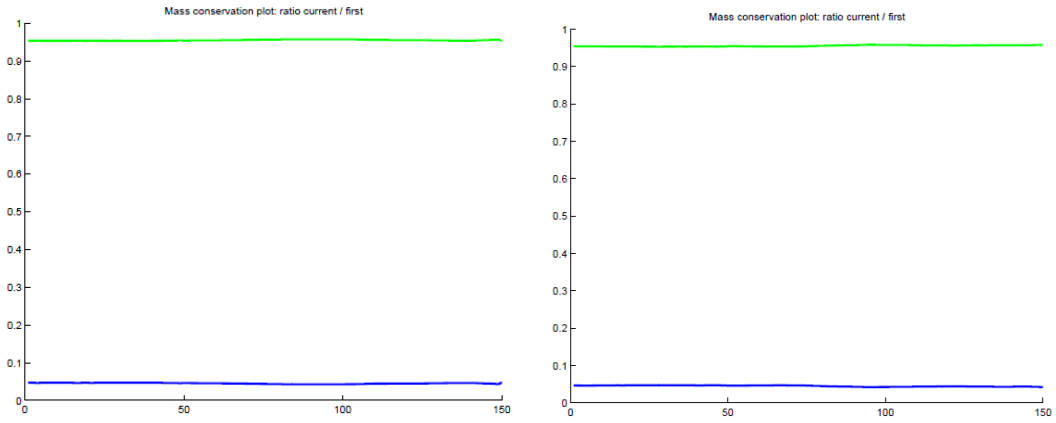

Figure 4.3 Mass conservation plots for flows with Reynolds number 10 & 100 at τ = 0.75

Chapter 5

Code Applications in Inkjet Printing Device

5.1 Background Study

There is a wide variety of actuation methods being adopted to eject the liquid droplet through the nozzle of the inkjet printing device. These methods include the most popular piezoelectric, the thermal bubble, the electro-static and the acoustic actuators. There has been a lot of numerical studies done in the formation of droplet for high quality printing from piezoelectric inkjet process with different model approaches. For instance, numerical simulations with level set projection method has been developed to carefully study all the fluid flow phenomena associated with inkjet by *Y. Suh et al.* [1] and *J. D. Yu et al.* [2]. These studies include the formation and the ejection of the droplet as well as the surface tension effect on the interface. In the research done by *Wu et al.* [9], a detailed study focusing on the performance by different shape of nozzle has been done. In addition, the dynamic contact angle model which captures the behavior of the liquid-gas-solid contact point has been considered in *Y. Suh et al.* [1].

Generally, the ink used for regular dye-based desktop printers are Newtonian while the pigment based printer used in industrial application are viscoelastic. Therefore, we can find in *Yu et al.*[3], detailed study with an algorithm developed to handle both Newtonian and viscoelastic fluids has been done.

In a piezoelectric inkjet process, liquid (ink) is ejected via the nozzle by a pressure pulse resulting from the displacement of the piezoelectric element. The pressure jump at the lower boundary of inkjet nozzle induced by the piezoelectric system drives the liquid to move through the nozzle and subsequently lead to the formation of droplets at the nozzle. A general inkjet print head with partially tapered nozzle from *Wu et al.* [9] is being schematically shown in Figure 5.7 with all dimensions shown in micro meter. However, for the initial simulation, we are only interested on how well the code performs on the separation of droplet, i.e. the interface capturing of the code.

5.2 Initial Simulations with different meshes

The initial simulation exercises started with the simplified axis-symmetric square nozzle inlet instead of a tapered one with different types of meshes generated with the ez4u mesh generator. This is to test if the setting of the model works on quadrilateral and triangular mesh as well as the effects of the different meshes on the code. For quadrilateral, both the structured and unstructured meshes are being considered.

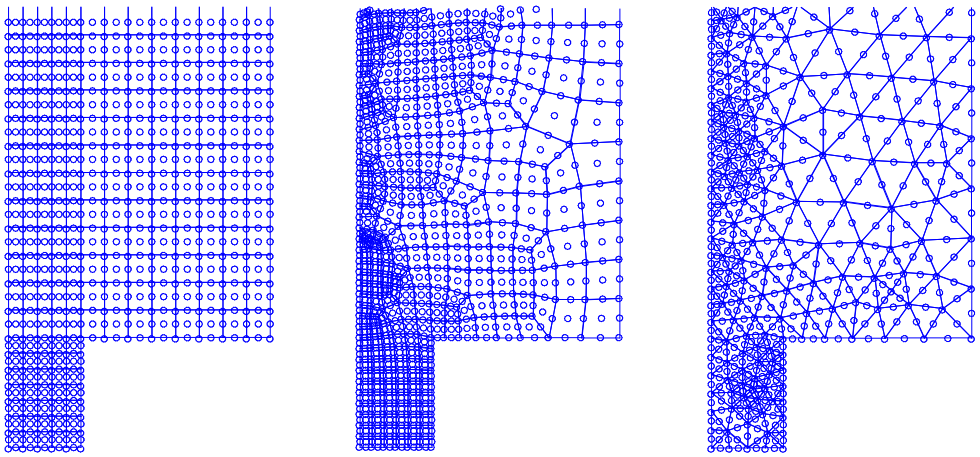

(A) 763 elements (B) 777 elements (C) 836 elements

Figure 5.1 Meshes for simplified geometry of the inkjet nozzle: (A) structured Q2Q1 mesh, (B) unstructured Q2Q1 mesh and (C) P2P1 mesh

Essentially, to generate a good mesh with lesser element we need to have local refinement on the interface instead of the whole long domain. It is easier to create an unstructured mesh with ez4u compared to structured mesh because of the geometry itself. Therefore, lesser elements can be produced for unstructured mesh compared to structured quadrilateral mesh while maintaining a relatively good mesh to capture the interface movement. Here, the meshes used to compare have a relatively same degrees of freedom as it is almost impossible to produce different types of mesh with the same amount of elements. In any case direct comparison of different mesh type cannot be done on a like for like basis. However the computational cost of both cases was similar.

For the trial velocity at the interface, a polygonal inflow velocity function $u_y(t)$ is used to define the maximum inlet velocity for each time step. This local distribution of the velocity is in space. Therefore, we have always an inflow velocity $u_y(t)$ at the centre of the nozzle (radius = 0) and a zero velocity at the nozzle wall. Between these two

conditions, a parabolic distribution is chosen to produce a droplet. Here, the positive velocity is intended to give some momentum to the fluid so that it would push forward and eject. After that, we imposed negative velocity to induce a back flow so that the fluid can be sucked back into the nozzle. However, due to the inertia and the instabilities, the ink which has been ejected could not move back but subsequently cause the column of ink to pinch and lead to the creation of the droplet.

In Figure 5.3, you can see that the ink is ejected through the nozzle and elongates with time to form a droplet. Then a negative velocity is imposed when the column of ink is still moving forward. This has caused necking to occur. This is clearly shown in Figure 5.3 (d) and later on the column of ink became thinner and thinner until it separated to form a first droplet. The results shown are qualitatively similar with the results published by *Y. Suh et al.* [1] in Figures 5.2 even though the nozzle shape is different. The ejection and elongation of ink column shown has been clearly captured in an axis-symmetric model.

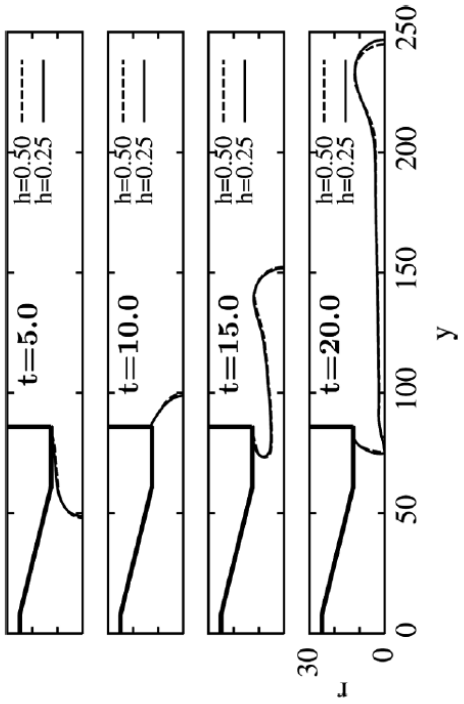

Figure 5.2 Ejection of droplet from inkjet nozzle in *Y. Suh et al.*

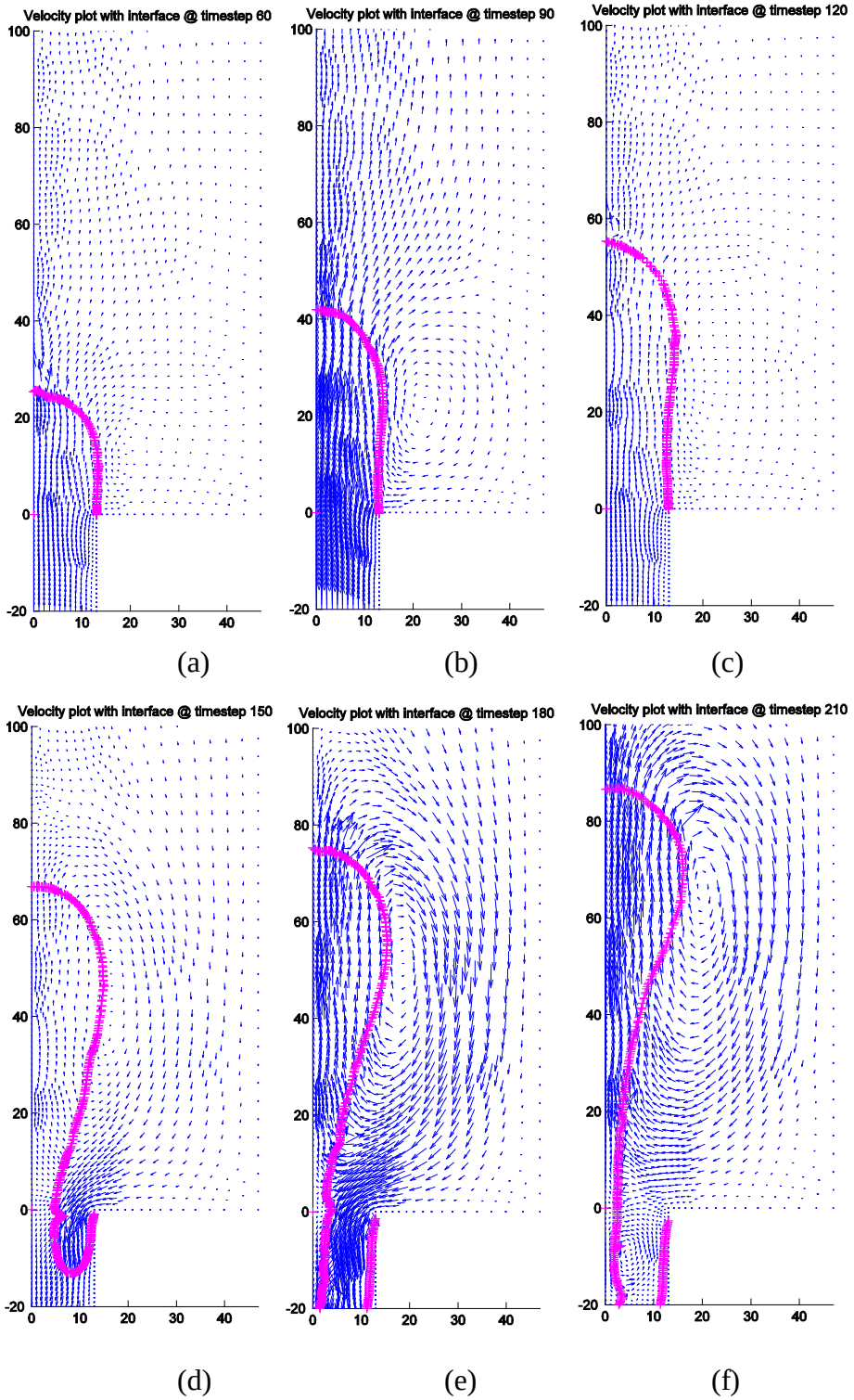

Figure 5.3 Results for simplified inkjet model with unstructured Q2Q1 mesh

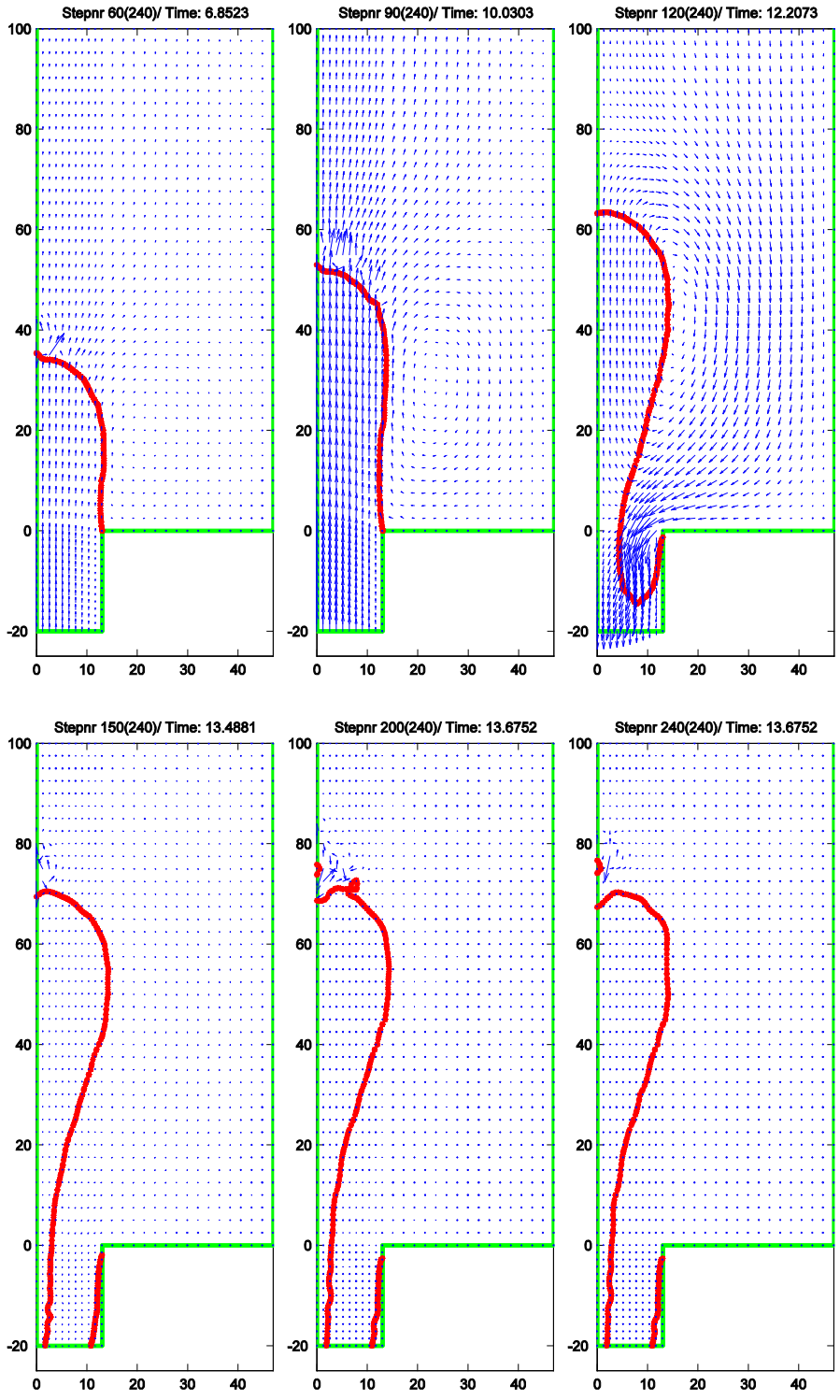

Figure 5.4 Results for simplified inkjet model with structured Q2Q1 mesh

5.2.1 Comparison of results for different meshes

From the results obtained from the simplified axis-symmetric model, we can already draw some conclusions from these initial results. As we can see from Figure 5.5, the results for unstructured quadrilateral mesh, the interface has been captured nicely and the droplet has ejected and separated. However, after separation, the interface became unstable in the vicinity of the interface separation as shown below.

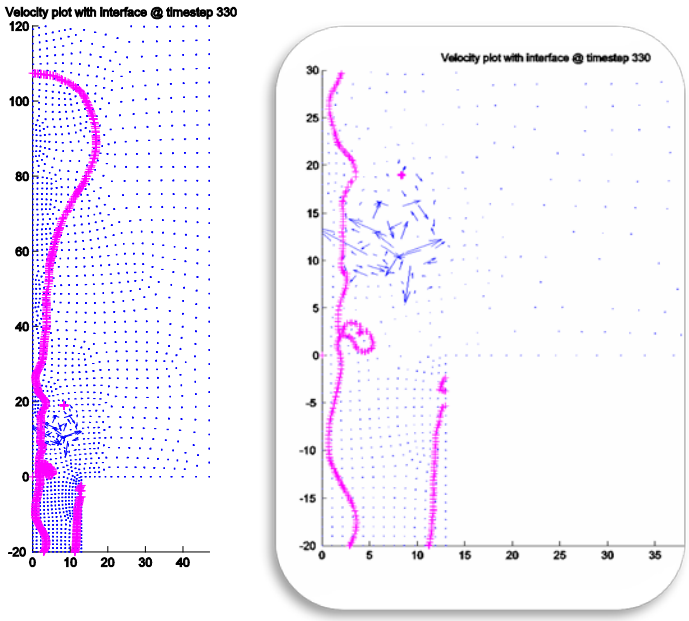

Figure 5.5 Interface plot at time step 330 for unstructured Q2Q1 with the zoom image for corrupted interface

Followed by the structured Q2Q1 mesh, we can see that the computation went well before the separation. However, once the interface separations took place, it lost its symmetric configuration. (Figure 5.6) This has shown that the axis-symmetric model has

not yet been implemented correctly. More efforts have to be instilled in this in aspect in order to be able to study axis-symmetric models later on.

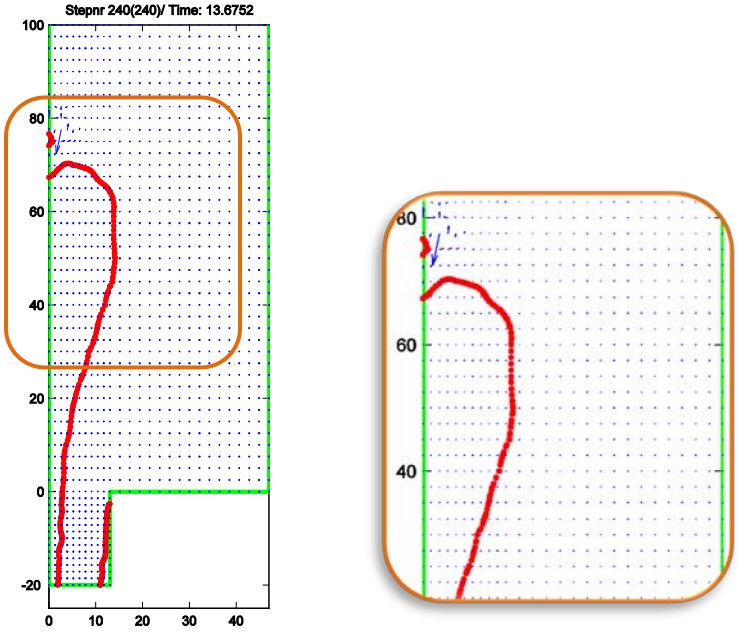

Figure 5.6 Interface plot at time step 240 for unstructured Q2Q1 with the zoom image to show non-symmetry

Lastly for the results obtained with unstructured triangular mesh, i.e. P2P1 elements were not successful. This setting was not able to capture the interface from the very beginning, even before the separation occurred. In addition, non-physical phenomenon where the interface separate at the front part of the droplet was observed. This has proven that we need to re-study the axis-symmetric model of this code as well as to have sufficient stabilization in order to capture the interface correctly after separation, especially when there are satellites at the tail of the droplet. Therefore, for further simulation, the evolution of droplet is captured in a two dimensional domain. However, it has to be aware that the meshes used for these initial computations are coarse and therefore the results may not be fully represented quantitatively at this stage.

5.3 2D model of Inkjet Nozzle

In the previous computations done with axis-symmetric model, the inaccuracy in capturing the interface was experienced. The situation has become worse when the separation of the ink happened. Therefore, a 2D model has been created (Figure 5.7) for further simulation by keeping the same general geometry as previous computation, but adapted the dimension from *Yu et al.* [2]. A pressure inflow has been imposed by *Yu et al.* [2] at the bottom of the nozzle head to simulate the effects of piezo-electric actuation. Due to the current limitations of the code, a pressure inflow model is yet to be implemented.

5.3.1 Model Description

For this simplified 2D model, we imposed no slip condition on the solid wall, i.e. zero velocity for normal and tangential component. This includes the liquid-gas-solid point mentioned in previous section as more study has to be done for the contact angle model. For outlet, a free slip condition is imposed with the horizontal velocity component set to zero and not prescribed value for the vertical component. Then, for inflow boundary condition, a time-dependant velocity profile of polygonal distribution $u_y(t)$ is adapted following the imposed inflow pressure in *Y. Suh et al.* [1].

Now, the diameter of nozzle used is 50 instead of 52 as in the axis-symmetric model. The ink-air interface has been initialized at $y = 0$. The same initial and boundary conditions from previous model are applied for all the computations with the maximum inflow velocity of $2.6\frac{\mu m}{\mu s}$ imposed at the center of bottom nozzle.

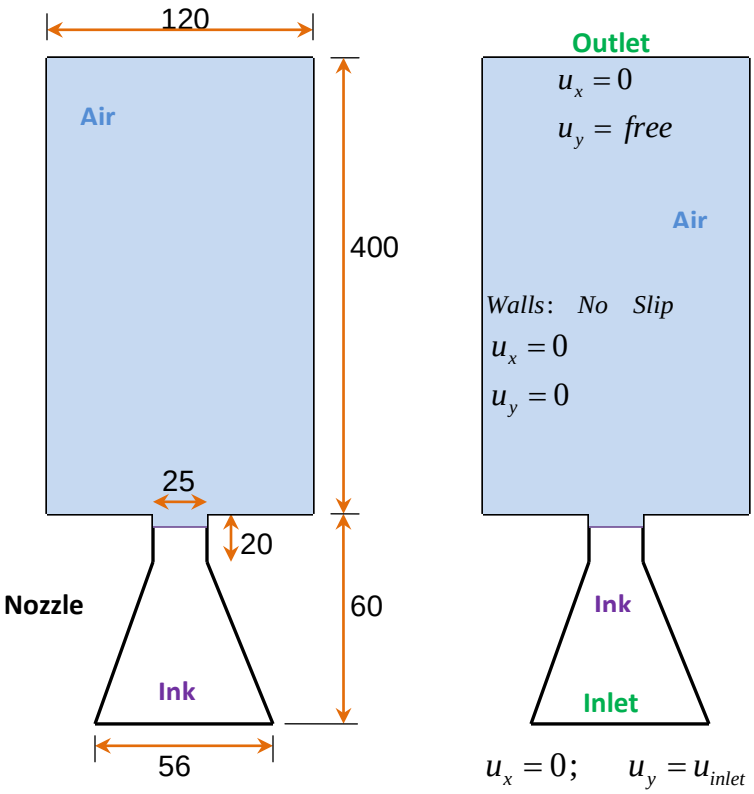

- All dimensions in micro meter

Figure 5.7 Geometry and Boundary conditions of the inkjet model

The Inflow velocity profile is shown in Figure 5.8 (b) below. As for the smoothing parameter ε mentioned at section 3.4, a value of 1×10^{-5} is applied. Finally, for all the related physical parameters, they are converted into microscopic scale.

Both the regular and locally refinement meshes with Q2Q1 and P2P1 are created to compare if the computation are mesh dependant. These meshes are created with more or less the same degree of freedom. They are shown in Figure 5.11 with their respective total number of nodes.

Viscosity : (kg/ms)	μ_1 μ_2	3.34×10^{-3} 1.775×10^{-3}
Density : (kg/m^3)	ρ_1 ρ_2	1070 1.225
Surface tension coefficient : (kg/m^2)	τ	0.032

(a)

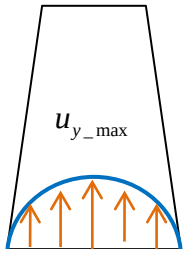

(b)

Figure 5.8 Physical parameters (a) and schematic Inflow velocity (b) for inkjet simulation

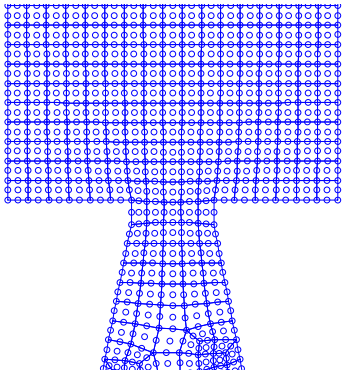

(a) 5045 nodes

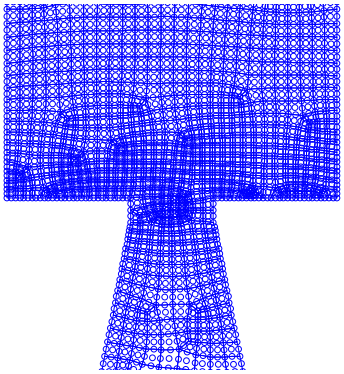

(b) 5381 nodes

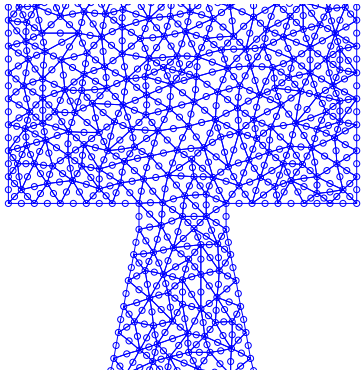

(c) 4951 nodes

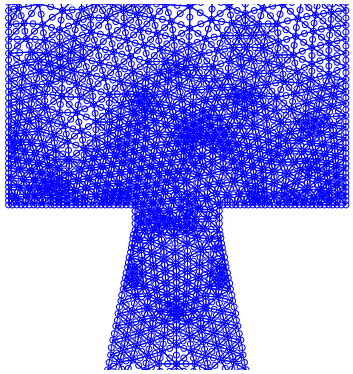

(d) 5217 nodes

Figure 5.9 Q2Q1 and P2P1 meshes: regular (a), (c) and locally refined (b) & (d)

5.4 Results for Q2Q1 and P2P1 mesh

Computations has been done with regular Q2Q1 and P2P1 mesh as well as respective locally refined mesh near the vicinity of the ink-air interface as shown in Figure 5.9. Results have been studied and compared in this section. From the results coming from Q2Q1 meshes, it is already shown that locally refinement near the vicinity of the interface yields better results.

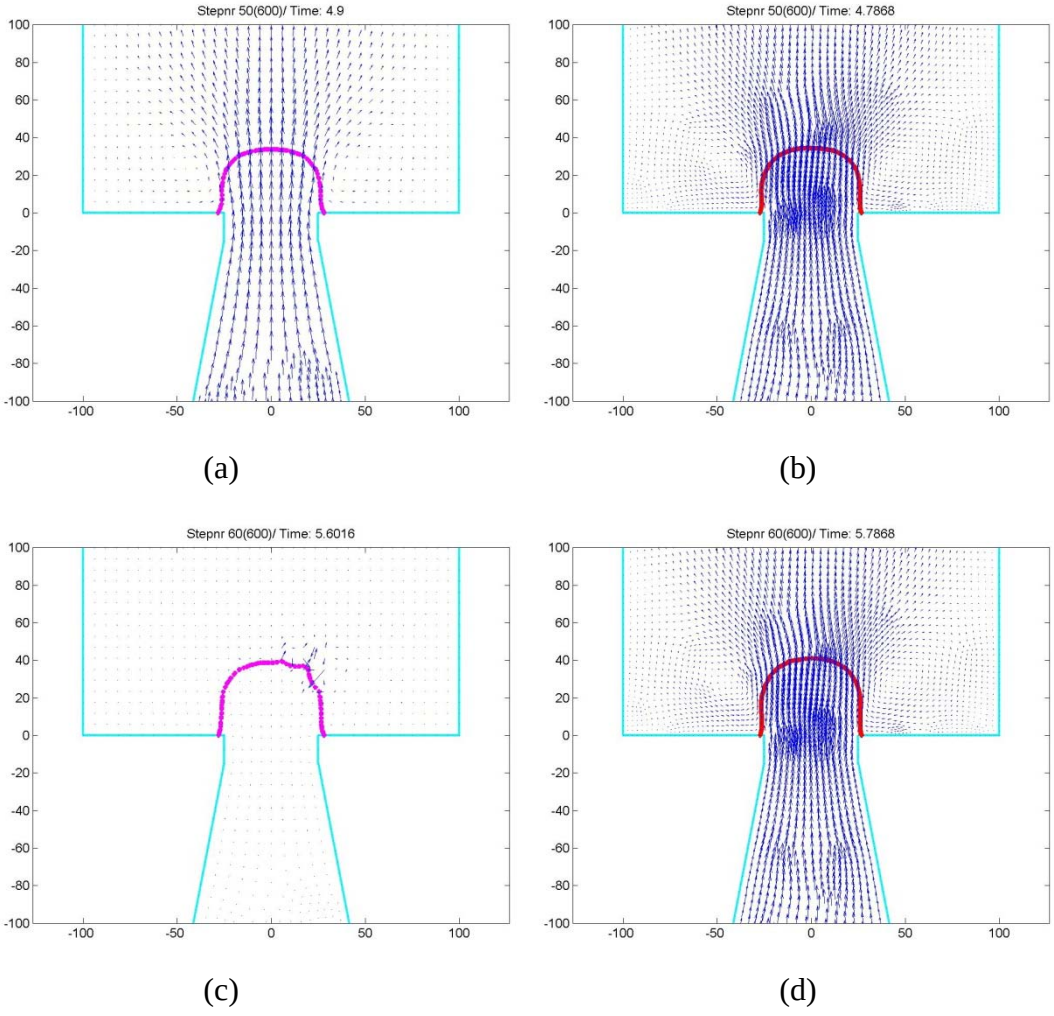

Figure 5.10 Velocity and interface plot for Q2Q1 regular (in pink) and locally refined mesh (in red)

This can be seen in Figure 5.10, where both the interfaces at time step 50 were captured nicely. The interface for regular mesh at time step 60 was started to corrupt while for the locally refinement mesh column of droplet has been formed and elongated until time step 210 before the interface get corrupted. It is found out that when the interface could not be tracked correctly then separation is impossible. However, the results shown suggest that parameters used and the imposed boundary conditions managed to give promising results with finer mesh but the stability has to be further enhanced. It is shown that stability is very important to track the interface prior to droplet separation.

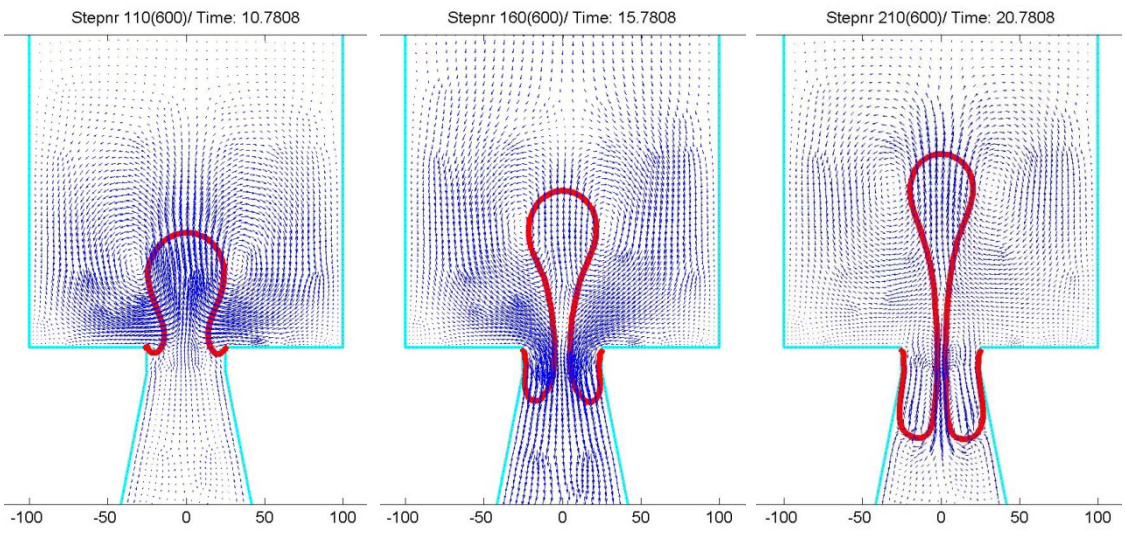

(a) (b) (c)

Figure 5.11 Velocity plot with interface for Q2Q1 locally refined mesh with $\varepsilon = 1e-5$

On the other hand, the results for the P2P1 mesh have as well shown that we need a very fine mesh to capture the interface correctly. For the computation with regular P2P1 mesh, the interface was corrupted just a few time steps after the computation was started. As for the locally refined P2P1 mesh, the results are shown in Figure 5.12 (a), (b) and (c)

for time step 100, 150 and 200 respectively. The column of ink has been formed and elongated nicely until time step 150 but the necking has been shorter compared with the results from Q2Q1 mesh. It can be seen that the interface at the liquid-gas-solid point has been the source of instabilities which lead to the corruption of the interface.

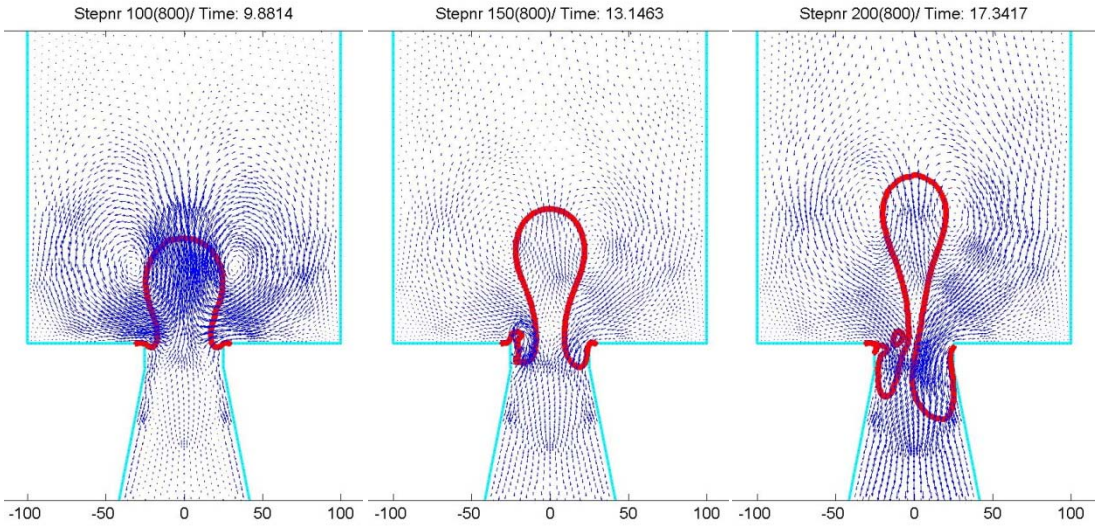

(a) (b) (c)

Figure 5.12 Velocity plot with interface for P2P1 locally refined mesh with $\varepsilon = 1e-5$

In addition, the model has lost its symmetry due to the presence of the instabilities coming from level set. Therefore, another attempt was made to see if the smoothing parameter could help in smoothing out the oscillations present due to the instabilities. A value of $\varepsilon = 1e-4$ is being applied to the elements. The results in Figure 5.13 has shown that this artificial diffusion really helped to smooth out the oscillations appearing due to the level set function and thus improve the stability of the current numerical scheme.

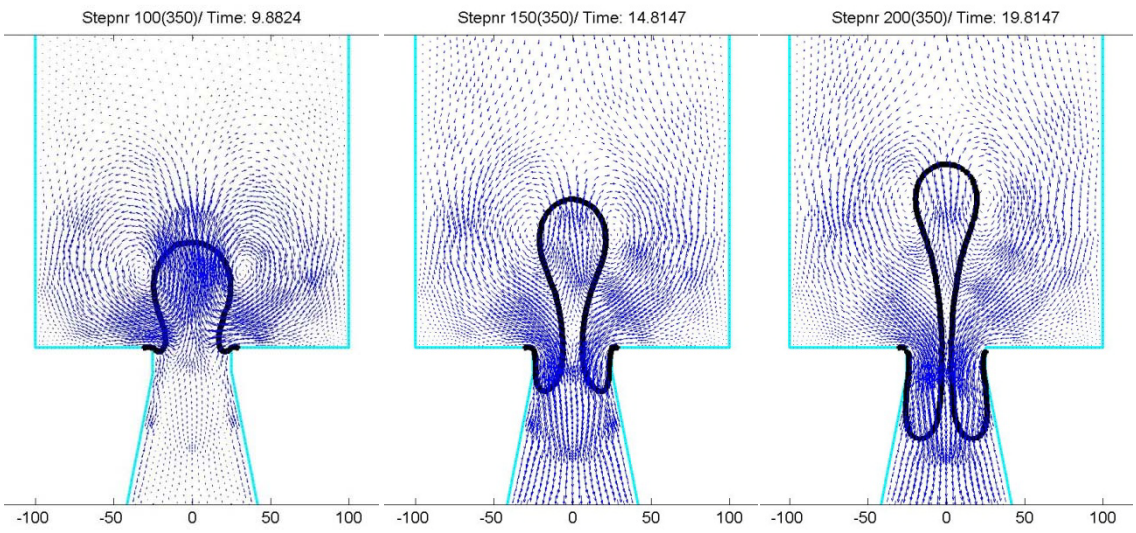

Figure 5.13 Velocity plot with interface for P2P1 locally refined mesh with $\varepsilon = 1e-4$

Besides, in order to show that the surface tension is indeed relevant in the droplet formation and ejection as well as playing a significant role in the stability of the solution, computations with lower and higher surface tension coefficient were being tried accordingly. As we could observe that reducing and increasing the surface tension coefficient, can impact the stability of the interface tracking. From Figure 5.14 below, one can notices that with a lower surface tension coefficient, i.e. lower surface tension force, the interface has lost its symmetry at an early stage which later on prevents a formation of droplet. As for a higher surface tension force, apparently no droplet can be formed through the nozzle as the surface tension force tends to retain the ink from being ejected.

Nevertheless, further study in setting the correct boundary condition for the three-phase contact point, i.e. the contact angle is also needed for the inkjet study. The results from *Wu et al.* and *Yu et al.* has been shown in Figure 5.15 and Figure 5.16 respectively to compare the results obtained.

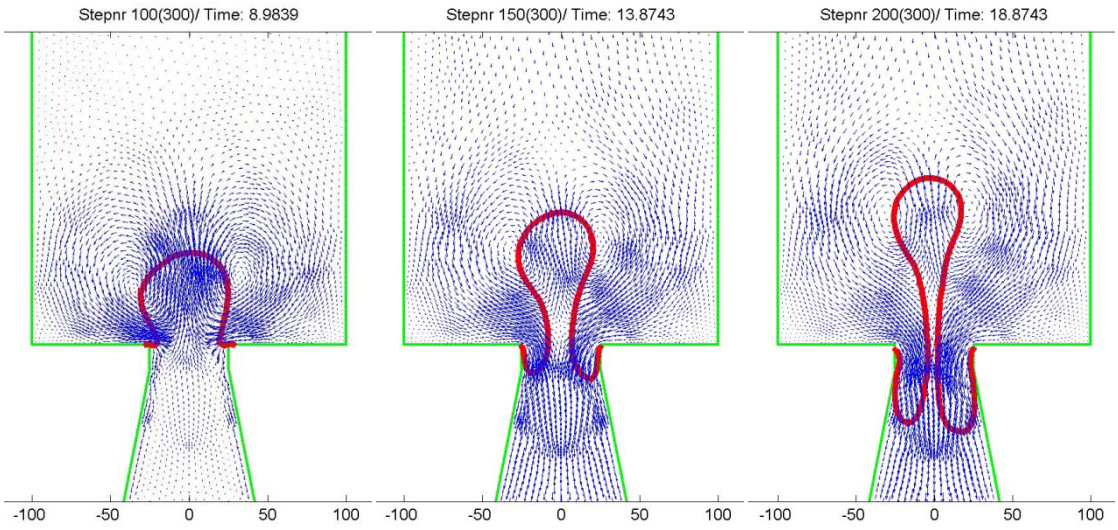

Figure 5.14 Velocity plot with interface for P2P1 locally refined mesh with $\tau = 30$

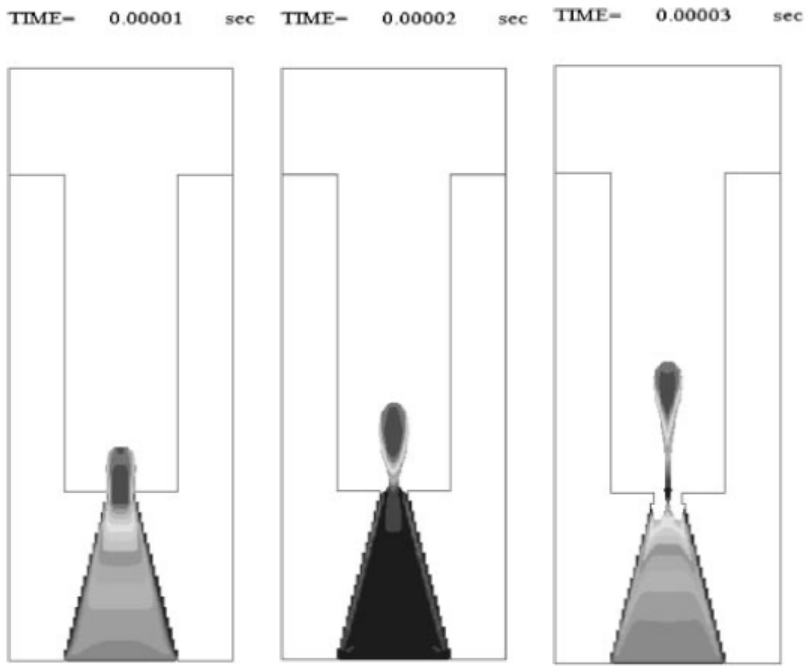

Figure 5.15 Droplet ejection at respective time shown from the publication of *Wu et al.*

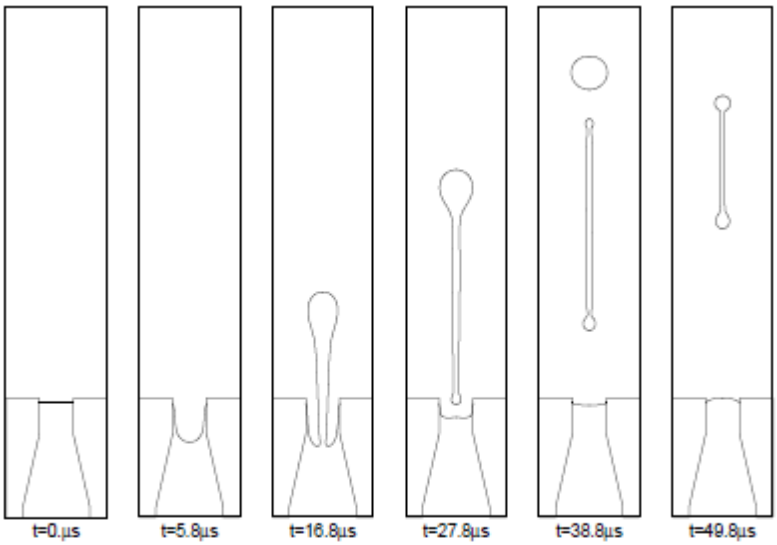

Figure 5: Droplet ejection (Newtonian).

Figure 5.16 Droplet ejection shown from the publication of *Yu et al.*

Chapter 6

Industrial Applications in Paper Drying Cylinder with Turbulator Bars

6.1 Background Study

The drying process of paper production is another industrial application of two fluid flows with moving interface, which is categorized under liquid film flows. In this case, the first fluid is the condensate formed inside the cylinder during the heat transfer process. The second fluid is a gas, i.e. steam that is supplied into the cylinder.

To start with this application, a brief introduction to how the paper drying process in industry is given. Steam cylinders are commonly used to dry the paper or board paper which is shown in Figure 4.2 below. Typically, a paper drying machine consists of 40 – 100 steam cylinders where the conduction takes place when steam is led into the rotating cylinders and sequentially dries the papers. As for the diameter of the cylinder, they normally range from 0.375m to 3.0 m.

Figure 6.1 Steam Cylinders in a paper drying factory

Inside each of the cylinders, as mentioned earlier, steam is led into the horizontally rotating cylinders and heats the inner surface of the cylinders which then dries the papers on the outer surface. However, when the cylinder rotates, there is a thin layer of condensate formed from the cooling steam which is caused by the friction and centrifugal force. This is not desired as the layer formed prevents the conduction between the steam and the cylinder surface. As a result, it acts as a barrier to heat transfer in this particular drying process.

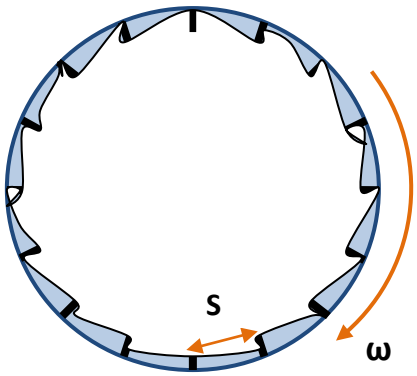

Figure 6.2 Schematic diagram of turbulator bars in a steam cylinder with water movements

In order to advance the heat transfer rate between the steam and the metal surface of cylinder, a suggestion has been given by Janne Nuutinen in his PHD thesis where the cylinder is divided by 15 metal bars on its inner surface into lengthwise container. The water sloshes within this rectangular section due to the changing of gravity and is held between the bars by centrifugal forces. The parameters has been studied and implemented so that the condensate sloshes as effectively as possible to increase the heat transfer via the turbulence created.

A clockwise frequency is considered for the rotating cylinder. The height of the turbulator bars is designed high enough to prevent condensate from flowing out of the rectangular section. The spacing of the bars is chosen based on the requirement of the occurrence of natural frequency so that sloshing occurs near natural frequency regardless the speed of the cylinder. This would cause the turbulence to take place as the sloshing caused by the natural frequency tends to be violent and chaotic.

6.2 Model Description

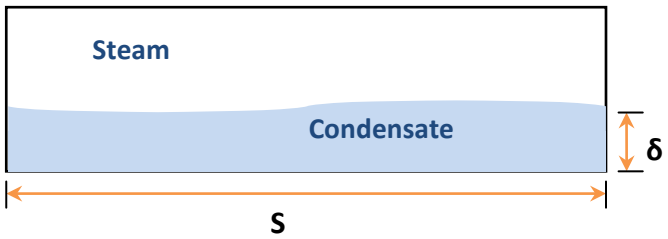

Figure 6.3 Simplified geometry of the condensate water sloshing between bars

The sloshing behavior of the condensate in each of the rectangular section is very important as the heat transfer rate is greatly depended on them. Therefore, the complexity of this problem has to be treated one by one. To simplify the problem, only one single

section is considered. The geometry is symmetric along the axis of the cylinder. The section is treated as a two-dimensional container without considering heat transfer as what we are interested in the first place is whether the desired turbulence effect takes place in the rectangular container.

The width of the container, **s**, i.e. the spacing of the bars is given by the equation below:

$$s = \pi\sqrt{R\delta}$$

where R is the cylinder radius and δ the depth of the condensate.

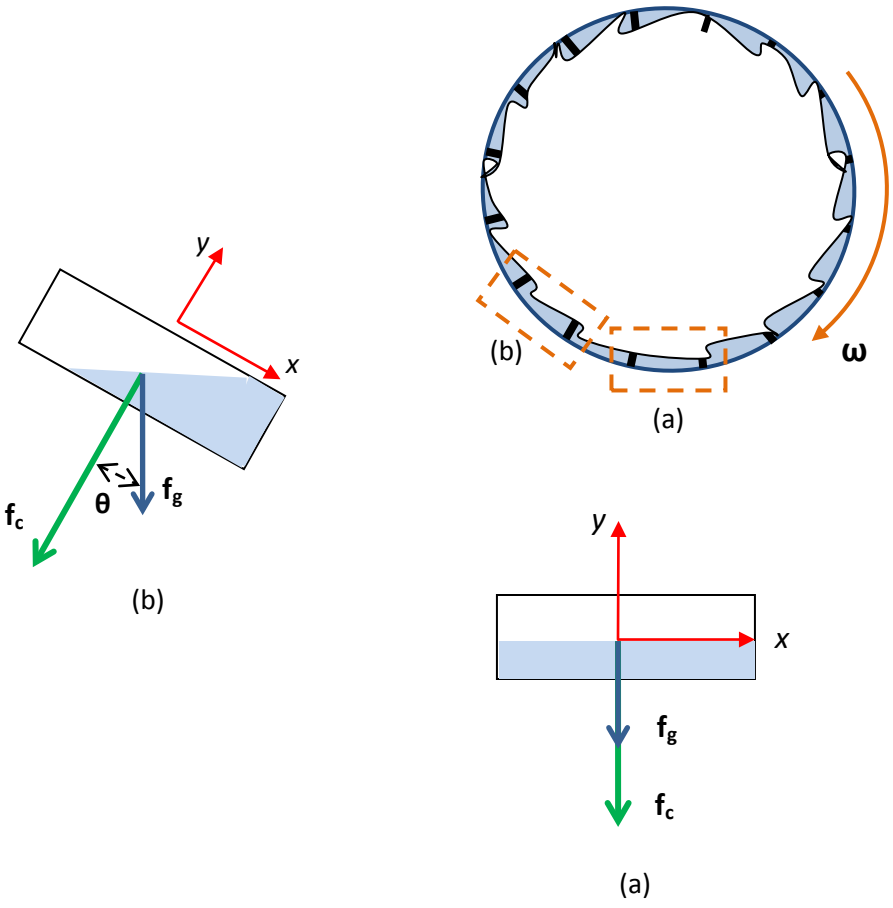

Figure 6.4 2D dimension of the rotating cylinder with the forces acting on rectangular box

Given that the cylinder is rotating with clockwise frequency where the frequency should be correspond to the resonant frequency. The centrifugal force is taken as negative y-direction which is outwards from the center of the cylinder. The centrifugal force and gravity force experienced by the rectangular container at rest (a), position after rotation θ (b) are illustrated in Figure 6.4.

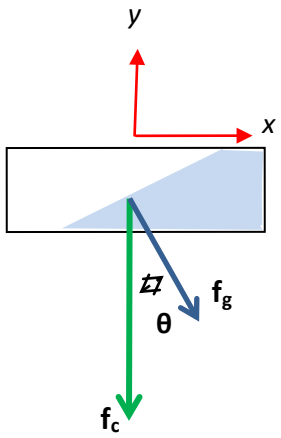

Figure 6.5 System coordinate for the rectangular box

The parameters and dimensions involved in this simplified model are shown below:

Height of bars = height of container	1.5	cm
Depth of water (when not sloshing), δ	1.0	cm
Length of container, s	30	cm
Cylinder inner radius, R	0.75	m
Gravity acceleration, g	9.81	ms^{-2}
Centrifugal acceleration, f_c	$-\rho\omega^2 R$	ms^{-2}
Frequency of rotation, f	4	Hz
Angular frequency, ω	$2\pi f$	rad/s
Gravity in x-direction, g_x	1g*sin(40*t)	ms^{-2}
Gravity in y-direction, g_y	1g*cos(40*t)	ms^{-2}

Table 6.1 Parameters used in the simplified model

Viscosity of air	:	μ_1	(kg/ms)	0.012×10^{-3}
Viscosity of condensate	:	μ_2		0.282×10^{-3}
Density of air	:	ρ_1	(kg/m^3)	0.645×10^{-3}
Density of condensate	:	ρ_2		1000

Table 6.2 Properties of condensate and air

6.3 Level set for the two-fluids

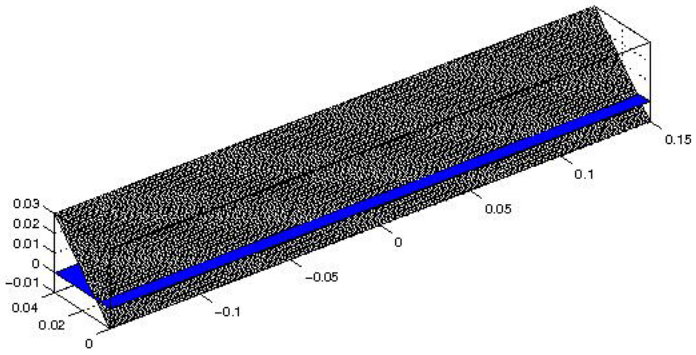

Figure 6.6 Level set plot for the condensate and air in the box

From Figure 6.6 above, the level set of the model is shown in isotropic view. We can see that the positive level set is defined for the first fluid, which is the air and the negative level set for the condensate at the bottom.

6.4 Results

The computation for the above model has been done with a mesh of 880 structured quadrilaterals with 80 elements in x-direction and 11 elements for y-direction. However, no promising results have been obtained for this test case. The air-condensate interface is not able to be captured well even with a very small time step used. Different values of smoothing parameters has been tried to see if it would improve the interface capturing, however, this effort was bound to failed. In Figure 6.7, there are oscillations at the interface on the right due to the presence of high velocities.

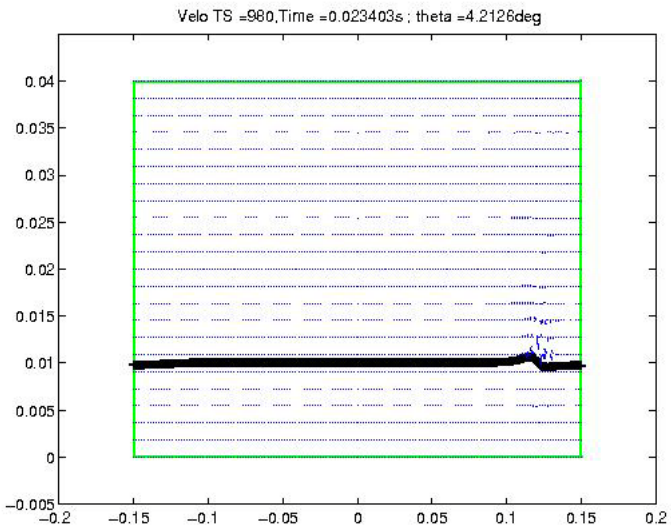

Figure 6.7 Velocity and interface plot for time step 980 at 0.0234s

Therefore, another try with denser fluids has been done to see if the big difference of viscosity between the condensate and the air is the cause to the big oscillations found at the interface. Glycerol and olive oil were chosen as the two-phase fluids for the subsequent computations.

Viscosity of glycerol	:	μ_1	(kg/ms)	0.081
Viscosity of olive oil	:	μ_2		1.49
Density of glycerol	:	ρ_1	(kg/m^3)	850
Density of olive oil	:	ρ_2		1126.1

Table 6.3 Properties of glycerol and olive oil

The computation for the aforementioned fluids has been done for frequency of 0.5 and 1.0. The velocity plots with rotation frequency of 0.5 are shown in Figure 6.8 at time steps 75, 200, 375, 475 and 650 with their respective angular position. The fluid moved to the right of the domain as expected and tends to stick to the wall due to the centrifugal forces. As for the results with rotation frequency of 1.0 shown in Figure 6.9, we can see that the fluid sticks to the wall more than the one with lower rotation frequency. This is because higher rotation frequency means higher centrifugal forces

The computation done could only shows that the viscosity of fluid has great influence on the interface capturing as well as the important of correct stability term. This has been shown that instabilities introduced in the previous computation with condensate and air is closely related to the viscosity difference of the two fluids. More time and efforts have to be put into this study in order to improve the robustness of the current numerical model. Once this issue is addressed, the next step in improving the paper drying cylinder model will be to reproduce the effect of the turbulator bars by introducing some periodic conditions between the upper parts of the lateral boundaries (and keeping wall boundary conditions in the lower part of the same boundaries). Then one could see the condensate flow from one rectangular section to another one. Finally one could include a turbulence model and one could observe and account for the turbulence generated by the turbulator Bars. At this stage one could then model the whole geometry and study the effect of the various rotational speeds.

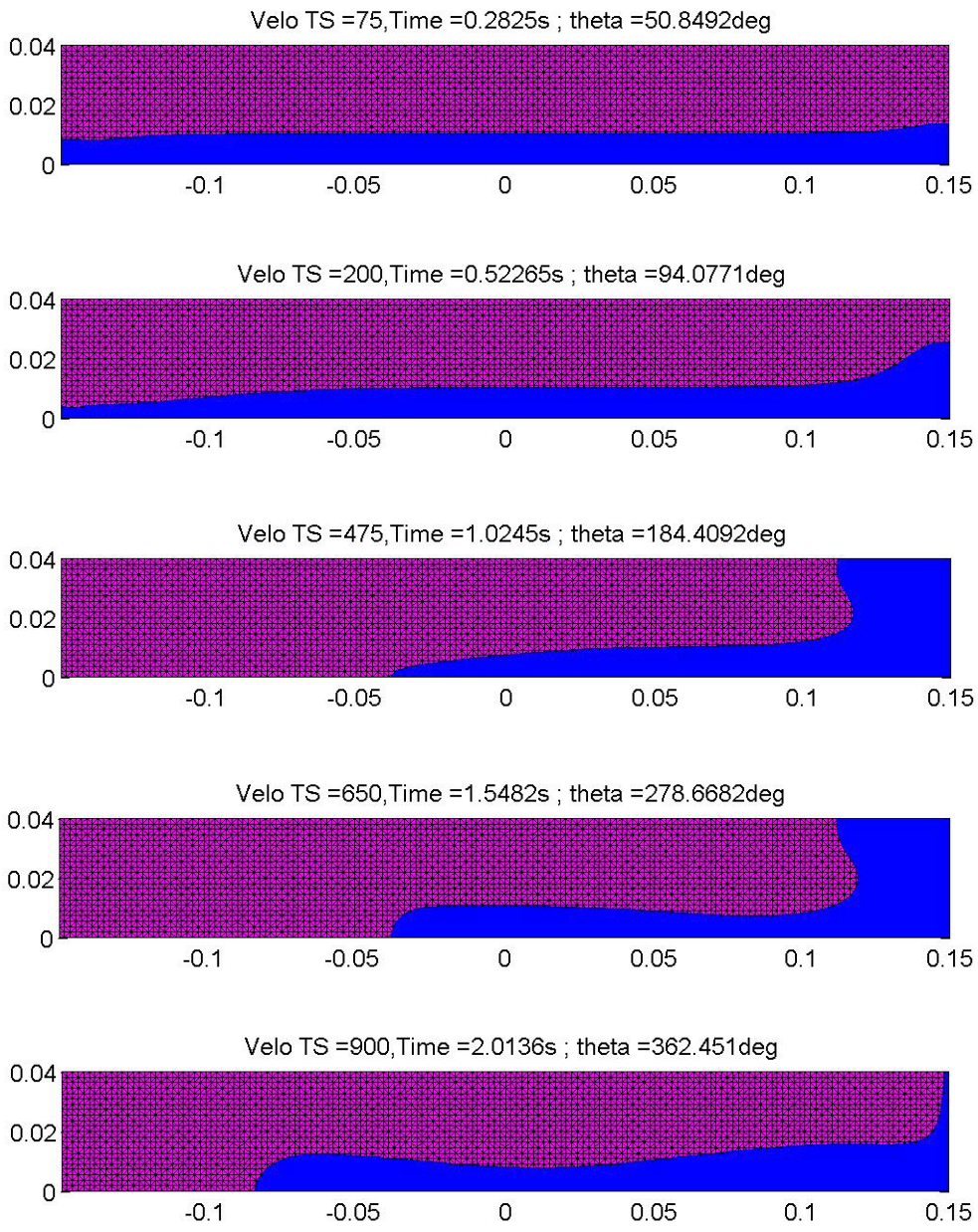

Figure 6.8 Interface plots for computation with glycerol and olive oil using f=0.5

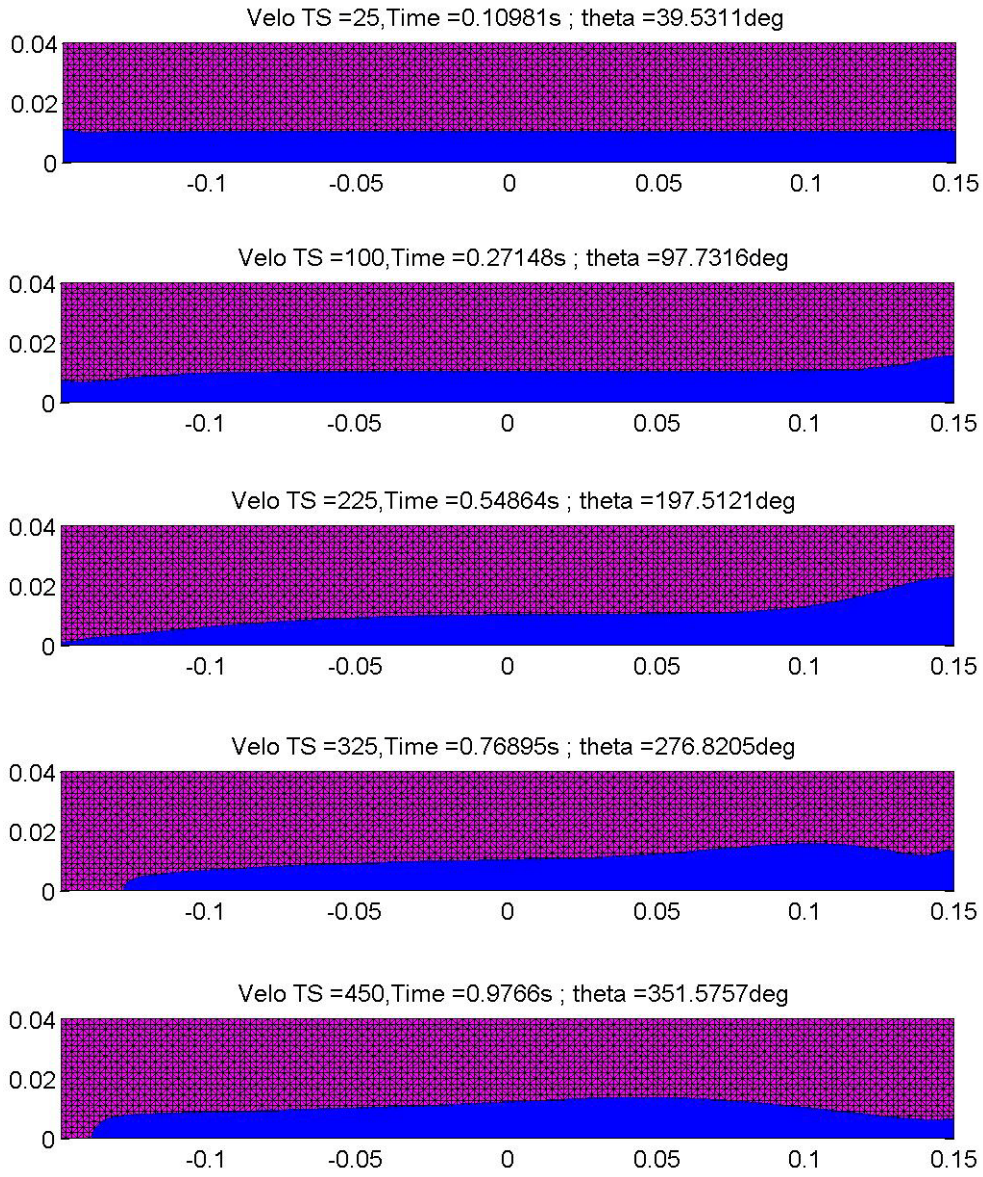

Figure 6.9 Interface plots for computation with glycerol and olive oil using f=1.0

Chapter 7

Conclusions

In the effort of solving the two-phase incompressible flows with surface tension, we have implemented the Extended Finite Element Method together with the front capturing level set method. Two industrial cases have been tested to evaluate the numerical approach, which is the inkjet printing and the paper dying cylinder with turbulator bars. The two models were being set up and tested with the numerical scheme implemented. Results has been post-processed and presented in this thesis.

Several important points arise from these computation results obtained. First and foremost for the inkjet problem, the results suggest that the computations are still mesh dependant. Better results were obtained with locally refined mesh at the vicinity of the interface. Non-physical phenomena like the satellite formation in front of the droplet disappear when a finer mesh is used with the same computation settings. Secondly, the stability of the interface capturing level set method has to be further studied and improved. Due to the fact that this is an explicit scheme, very small time step is needed in moving the level set to ensure the stability. Even though the droplet was formed and elongated, the

separation of the droplet are still dependant on the stability of the level set interface tracking scheme. The smoothing parameter is increased to obtain a bigger artificial diffusion over the interface. This has greatly reduced the oscillations in the level set and improved the interface tracking during the evolution of droplet of computation with P2P1 mesh shown in Appendix A and B. The reason is because when the ink column became very thin moments prior to separation, the capture of the interface became difficult and this scheme seems to struggle to locate the interface. Therefore, a more robust scheme has to be implemented to capture the interface more effectively. Besides, the results from inkjet problem have also shown that the surface tension is indeed relevant in the droplet formation and ejection, but also play a role in the stability of the solution, as we could observe that reducing and increasing the surface tension coefficient, can impact the stability of the interface tracking.

For the second case, i.e. paper drying cylinder with turbulator bars, problem has been simplified to a rectangular box by applying the relevant forces, operating and boundary conditions. The problem has shown the limitation of the implemented numerical scheme in handling the condensate and air interface tracking. Given the operating conditions, the interface capturing was bound to fail as high oscillations occurred at the interface and corrupted the results. Again, a more rigorous study about the stability of the current numerical scheme is needed. Computations with two denser fluids have been carried out to see how the interface evolves with time. The results shown are promising as the fluids behave as expected. However these results cannot be considered as conclusive with respect to the original application of the paper drying cylinder, therefore the current study indicates that more time and efforts are needed to further develop the code in order to solve this problem as well as handle more complicated industrial problem.

Appendices

Appendix A

Velocity and Interface plot for Inkjet model with P2P1 locally refined mesh with $\tau = 32$ and $\varepsilon = 1e-5$

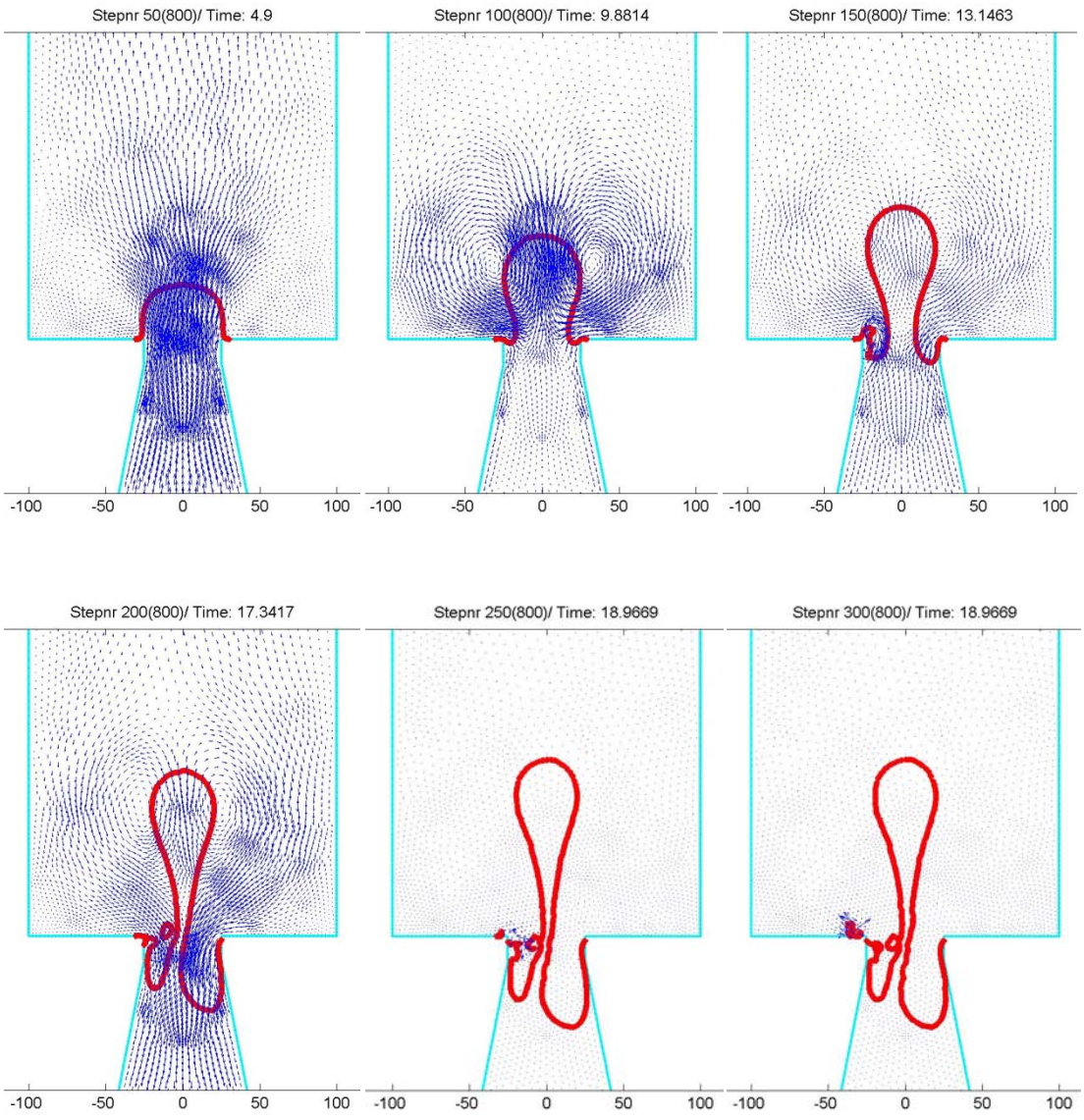

Appendix B

Velocity and Interface plot for Inkjet model with P2P1 locally refined mesh with $\tau = 32$ and $\varepsilon = 1e-4$

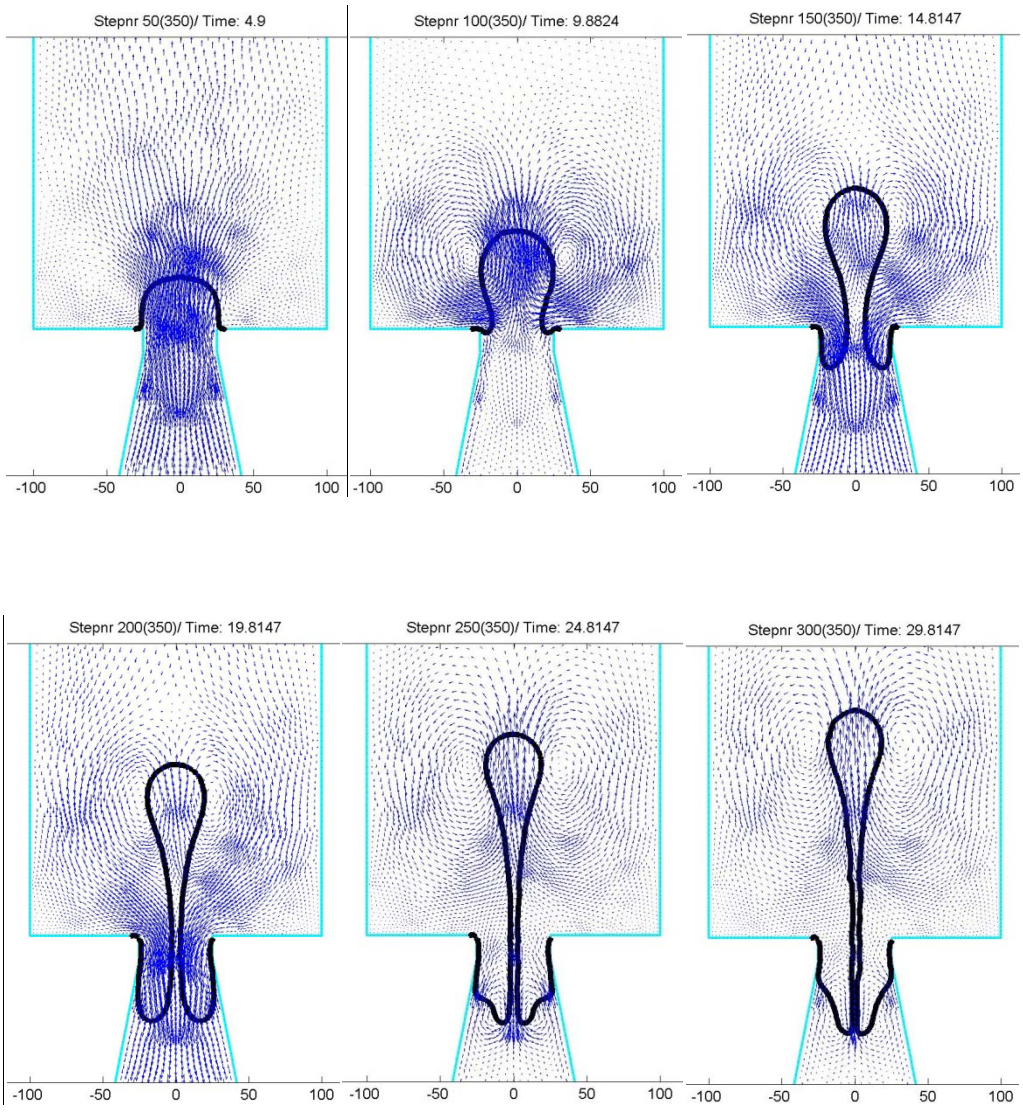

References

1. Y. Suh and G. Son. A Sharp-interface Level Set Method for Simulation of Piezoelectric Inkjet Process. *Numerical Heat Transfer B*, vol. 55: 295-312, 2009.
2. J. D. Yu, S. Sakai, and J. Sethian. A Coupled Level Set Projection Method Applied to Ink Jet Simulation.
3. J. D. Yu, S. Sakai, and J. Sethian. Two-phase Viscoelastic Jetting. *J. Comput. Phys.*, vol 220: pp. 568-585, 2007.
4. J. Chessa and T. Belytschko. An Enriched Finite Element and Level Sets for Axisymmetric Two-phase flow with surface tension. *I. Numer. Meth. Engng.* vol. 58: pp. 2041-2064, 2003.
5. S. Zlotnik, P. Díez, M. Fernández, J. Vergès. Numerical modeling of tectonic plates' subduction using X-FEM. *Comp. Methods Appl. Mech. Engrg.*, vol. 196: pp. 4283-4293, 2007.
6. A. Smolianski. Finite Element/Level-Set/Operator-Splitting (FELSOS) Approach for Computing Two-Fluid Unsteady Flows with Free Moving Interfaces.
7. E. Marchandise, J.-F. Remacle. A stabilized Finite Element Method using a discontinuous Level Set Approach for solving Two Phase Incompressible Flows. *Journal of Computational Physics,* vol. 219, no.2 : pp. 780-800, 2006.
8. J. Nuutinen, Heat Transfer inside a Paper Drying Cylinder with Turbulator Bars – Technical Report, 2009.
9. H-C. Wu, H-J. Lin, Y-C. Kuo, W-S. Hwang. Simulation of Droplet Ejection for a Piezoelectric Inkjet Printing Device. *Materials Transactions,* vol. 45, no. 3: pp. 893-899, 2004.
10. S. Zlotnik. Numerical modeling of transient multiphase thermo-mechanical problems: Application to the oceanic lithosphere, 2008.
11. S. Groß, V. Reichelt, A. Reusken. A finite element based level set method for two-phase incompressible flows. *Comput. Visual Sci.* vol. 9: pp. 239-257, 2006.
12. E. Aulisa. Modeling two-phase flows with a FEM solver of the Navier-Stokes equations and an area preserving front tracking method for the interface advection.

13. Y. C. Chang, T. Y. Hou, B. Merriman, S. Osher. A Level Set Formulation of Eulerian Interface Capturing Methods for Incompressible Fluid Flows. *Journal of Comp. Physics*, vol. 124: pp. 449-464, 1996.
14. G. Compère, E. Marchandise, J-F. Remacle. Transient adaptivity applied to two-phase incompressible flows. *Journal of Comp. Physics*, vol. 227: pp. 1923-1942, 2008.
15. E. Marchandise, P. Geuzaine, N. Chevaugeon, J-F. Remacle. A stabilized finite element method using a discontinuous level set approach for the computation of bubble dynamics. *Journal of Comp. Physics*, vol. 225: pp. 949-974, 2007.
16. S. Groß, A. Reusken. An extended pressure finite element space for two-phase incompressible flows with surface tension. *Journal of Comp. Physics*, vol. 224: pp. 40-58, 2007.
17. S. Popinet, S. Zaleski. A front-tracking algorithm for accurate representation of surface tension. *Int. J. Numer. Meth. Fluids*, vol. 30: pp. 775-793, 1999.
18. J. Chessa, T. Belytschko. An Extended Finite Element Method for Two-phase Fluids. *Journal of Applied Mechanics*, vol. 70, 2003.
19. C. Devals, M. Heniche, F. Bertrand, P. A. Tanguy, R. E. Hayes. A two-phase flow interface capturing finite element method. *Int. J. Numer. Meth. Fluids*, vol. 53: pp. 735-751, 2007.
20. Y. Suh and G. Son. A Level-Set Method for Computation of Droplet Motion in An Inkjet Printing Process.
21. J. Donea, A. Huerta. Finite Element Methods for Flow Problems, Wiley, Chichester, West Sussex PO19 8SQ, England, 2002.